# Synoptic responses to mountain gravity waves encountering directional critical levels

Armel MARTIN and François LOTT

Laboratoire de Météorologie Dynamique du CNRS,

Ecole Normale Supérieure,

24, rue Lhomond, 75235 PARIS cedex 05, France

June 20, 2006

## Abstract

A heuristic model is used to study the synoptic response to mountain Gravity Waves (GWs) absorbed at directional critical levels. The model is a Semi-Geostrophic version of the Eady model for baroclinic instability adapted by Smith (1984) to study lee cyclogenesis. The GWs exert a force on the large-scale flow where they encounter directional critical levels (Shutts 1995). This force is taken into account in our model, and produces Potential Vorticity (PV) anomalies in the mid-troposphere.

First, we consider the case of an idealized mountain range such that the orographic variance is well separated between small-scale and large-scale contributions. In the absence of tropopause, the PV produced by the GWs force has a surface impact that is significant compared to the surface response due to the large scales. For a cold front, the GWs force produces a trough over the mountain and a larger amplitude ridge immediately downstream. It opposes somehow to the response due to the large scales of the mountain range, which is anticyclonic aloft and cyclonic downstream. For a warm front, the GWs force produces a ridge over the mountain and a trough downstream, hence it reinforces the response due to the large scales.

Second, we verify the robustness of the previous results, by a series of sensitivity tests. We change the specifications of the mountain range, and of the background flow. We also repeat some experiments by including baroclinic instabilities, or by using the Quasi-Geostrophic approximation. Finally, we consider the case of a small-scale orographic spectrum representative of the Alps.

The significance of our results is discussed in the context of GWs parameterization in the General Circulation Models. Our results may also help to interpret the complex PV structures occurring when mountain gravity waves break in a baroclinic environment.

## 1   Introduction

The large-scale flow response to the breaking of vertically propagating gravity waves (GWs) has been the subject of many studies during the last 40 years. They follow the

seminal works of Eliassen and Palm (1961) and Bretherton (1969), which have shown that mountain GWs induce a net transfer of momentum from the ground toward the atmosphere. The importance of mountain GWs for the atmospheric circulation is now well established. The parameterization of mountain GWs in General Circulation Models (GCMs) reduces the cold bias these models present near the tropopause in the Northern Hemisphere mid-latitudes (Boer et al. 1984, Palmer et al. 1986, McFarlane 1987). More recent parameterizations of Subgrid-Scale Orography (SSO) include trapped lee-waves (Miller et al 1989) and nonlinear low level flow blocking (Lott and Miller 1997, Scinocca and McFarlane 2000), which both reduce biases in the low-level winds.

Although SSO parameterizations are often evaluated by looking at systematic errors on the zonal mean flow, they also influence non-zonal planetary scale patterns. For these patterns, it is noteworthy that the SSO parameterizations are not necessarily helpful, unless they permit that the SSO force has a substantial component in the direction perpendicular to the low-level flow (Lott 1999, Webster et al. 2003). This component can have three origins: (i) the anisotropy of the mountains (Phillips 1984, Scinocca and McFarlane 2000, Webster et al 2003); (ii) the fact that the mean orography in large-scale models does not produce enough vortex compression (Smith 1979; Lott 1999); and (iii) the presence of directional critical levels encountered by the GWs (Shutts, 1995). In this last circumstance, the orientation of the force with respect to the background flow is a consequence of the fact that a monochromatic GW encounters a critical level where the background wind is perpendicular to its horizontal wave-vector. The GW is then absorbed, provided that the background flow Richardson number is below 0.25 at this altitude (Booker and Bretherton, 1967). Since the momentum flux associated with a monochromatic GW is parallel to its horizontal wave-vector, aloft an isolated mountain the selective absorption of one GW at each level results in a force perpendicular to the wind at the same altitude. Note that this effect is the result of a vertical shear, and is distinct from the effects of horizontal variations in the background flow which can modify the horizontal wave-vector itself (Bühler and McIntyre, 2005).

Another large scale process related to mountains is lee cyclogenesis, for which various dynamical mechanisms were proposed. The local triggering of standing or transient Eady or Rossby edge waves (Smith 1984, 1986; Davis, 1997), the low-level modification of pre-existing large scale unstable baroclinic mode (Pierrehumbert, 1985; Speranza et. al, 1985; Fantini and Davolio, 2001), or the cold-front distortion by low-level blocking (Mesinger and Pierrehumbert, 1986; Schär, 1990; Gross, 1994), are some of these processes. Actually, they are not exclusive, and this variety of theories illustrates the complexity of this problem. Accordingly, few studies have addressed the role of small scale orography on it.

Nevertheless, as the resolution of regional models increases, the synoptic scales are nowadays rather accurately represented. Besides, quite recently the forecast models began to solve together the synoptic scales and the mesoscale dynamics, including the upper-level GWs and the low-level PV banners appearing downstream of the individual mountain peaks (Hoinka et al, 2003; Liniger and Davies, 2003; Schär et al, 2003; Flamant et al, 2004; Jiang and Doyle, 2004). This recent progress in numerical modeling appeals for a better understanding of the impact of the small scale dynamics onto the synoptic flow, which is by the way one of the central objectives of the Mesoscale Alpine Program (MAP, Binder and Schär 1996, Bougeault et al. 2001). It is also in this context that Aebischer and Schär (1998) have suggested that the low-level cyclonic PV generated along the southwestern flank of the Alps could help to trigger lee cyclogenesis.

Although the interaction between mesoscale and synoptic-scale dynamics has been addressed during MAP, by means of either direct field measurements or numerical simulations, relatively few theoretical studies address this problem. It is nevertheless chal-

lenging for at least three reasons. First, the net force due to the breaking GWs acts over a domain which horizontal scales correspond to Rossby numbers of order 1 or larger. In this case, the large-scale response to the GWs is not entirely balanced but also contains re-emitted inertio-gravity waves (Scavuzzo et al. 1998, Lott 2003). Second, in the mid-troposphere the mountain GWs have little chance to break if the wind increases unidirectionaly, because the stationary waves vertical wavenumber decreases with altitude. Nevertheless, in the presence of fronts, many GWs can be absorbed at directional critical levels in the mid-troposphere (Shutts 1995) and break thereafter (Broad, 1999). The effect of this process on the large scale flow has never been evaluated. Third, a force that is everywhere perpendicular to the background wind can produce dipolar PV banners with an unusual structure.

This paper presents a theoretical model of the large-scale effect of the GWs generated by an idealized front passing over a mountain range. This model accounts for the GWs through the large-scale momentum deposit they induce where they encounter critical levels, in the mid-troposphere. For this purpose, we adopt a Semi-Geostrophic (SG) version of Smith's model (1984) of lee cyclogenesis in which we include a GWs force following Shutts (1995). The use of a balanced formalism here is supported by Lott (2003) which has shown by direct 2D simulations that after 12hrs typically, the balanced part dominates the inertio gravity waves part in the total response to GWs absorption at a critical level. In this framework, we analyze the surface response associated with the PV anomaly produced by the GWs force, and compare this response with that due to the smooth large-scale mean orography.

The plan of the paper is as follows. In Section 2 we present the model. In Section 3 we analyse the case of a cold front interacting with an idealized complex mountain range in the absence of tropopause. In Section 4 we describe the warm front case. In Section 5 we compare the Quasi-Geostrophic (QG) response with the SG response, we present some sensitivity tests to the altitude at which the gravity waves interact with the background flow, and we analyse the influence of the tropopause (which introduces unstable baroclinic modes). In Section 6 we present the results for orographic spectra representative of the Alps. Section 7 is a summary and a discussion of the implications of our results to the parameterization of mountain GWs in GCMs, or to the interpretation of the PV patterns produced in the mid-troposphere when a front crosses a mountain range.

## 2 Model
### 2.1 Equations for the large scale flow

A central assumption of our model is that the power spectrum of orography shows a clear separation between the large scales and the small scales. This permits to study separately the synoptic dynamics and the GWs dynamics. Although this separation is not valid in reality, it is implicitly assumed in SSO parameterization schemes. For this assumption to be valid, we adopt in Sections 3, 4, and 5 an idealized mountain range profile given by,

$$h(\mathbf{x}) = H_0 \, e^{-\frac{x^2+y^2}{2L^2}} \left(1 + \cos(\mathbf{k}_w \mathbf{x})\right) = \mathcal{H}(\mathbf{x}) \left(1 + \cos(\mathbf{k}_w \mathbf{x})\right), \tag{1}$$

where $\mathbf{k}_w = k_w \mathbf{e}_x + l_w \mathbf{e}_y$. In Eq. (1), $L$ is the characteristic large scale, $\mathbf{k}_w$ is the dominant horizontal wavenumber associated with the small scales, $2H_0$ is the maximum altitude of the mountain range and $\mathcal{H}(\mathbf{x})$ is the large scale orography profile, that is the envelope of the ridges (Fig. 1a,b).

In the linear context, and in the absence of critical levels, the large scale effect of the GWs forced by $h' = \mathcal{H}(\mathbf{x}) \cos(\mathbf{k}_w \mathbf{x})$ is very small if $k_w L \gg 1$. Nevertheless, if the GWs encounter directional critical levels (Fig. 1c), they are absorbed and can deposit the

momentum they transport. For the large scale flow, this effect can be translated into a force per unit mass (see subsection 2.3 and Appendix),

$$\boldsymbol{\mathcal{F}}(\mathbf{x}, z) = \mathcal{F}(\mathbf{x}, z)\, \mathbf{e}_x + \mathcal{G}(\mathbf{x}, z)\, \mathbf{e}_y \ , \tag{2}$$

whose impact adds to that of the large scale orography profile $\mathcal{H}(\mathbf{x})$.

To study the response to $\boldsymbol{\mathcal{F}}$ and $\mathcal{H}$, we adopt the Boussinesq approximation and consider an idealized front such that the background wind $\mathbf{U}$ and the potential temperature $\Theta_b$ have uniform shears:

$$\mathbf{U}(z) = U(z)\, \mathbf{e}_x + V_0\, \mathbf{e}_y = (U_0 + \Lambda z)\, \mathbf{e}_x + V_0\, \mathbf{e}_y \ , \tag{3}$$

$$\Theta_b(y, z, t) = \theta_r + \theta_{0z}.z + \Theta_y.y + \theta_{ad}(t) \ . \tag{4}$$

In Eqs. (3)-(4), $V_0$ is the surface wind, $\Lambda$ is the vertical wind shear, $\theta_r$ is a constant reference temperature, $\theta_{0z}$ is the vertical stratification, $\Theta_y$ is the cross front potential temperature gradient, and $\theta_{ad}(t)$ is the uniform change in potential temperature associated with the advance of the front. In this framework, the constant Brunt Vaïsala frequency $N$, $\Theta_y$ and $\theta_{ad}(t)$ can be written

$$N^2 = \frac{g\,\theta_{0z}}{\theta_r} \ , \quad \Theta_y = -\frac{\Lambda f \theta_r}{g} \quad \text{and} \quad \theta_{ad}(t) = -V_0\, \Theta_y\, t \ . \tag{5}$$

In Eqs. (5), the thermal wind balance relates $\Theta_y$ to $\Lambda$, $f$ is a constant Coriolis parameter, and $g$ is the gravity constant.

If we assume that the forcings $\mathcal{F}$, $\mathcal{G}$ and $\mathcal{H}$ are of small amplitude and have a characteristic horizontal scale $L$ such that the large scale Rossby number $\frac{V_0}{fL}$ is near or below 1, the response of the flow can be evaluated using a forced and linearized version of the hydrostatic SG equations given in Hoskins (1975):

$$
\begin{aligned}
(\partial_t + \mathbf{U}\nabla)\, u_g + w\Lambda - fv + \partial_x \phi &= \mathcal{F} &\text{(a)}\\
(\partial_t + \mathbf{U}\nabla)\, v_g + fu + \partial_y \phi &= \mathcal{G} &\text{(b)}\\
\partial_z \phi &= g\theta/\theta_r &\text{(c)}\\
(\partial_t + \mathbf{U}\nabla)\, \theta + v\Theta_y + w\theta_{0z} &= 0 &\text{(d)}\\
\partial_x u + \partial_y v + \partial_z w &= 0 &\text{(e)}
\end{aligned}
\tag{6}
$$

In Eqs. (6), $(u, v, w)$ are the components of the wind perturbation, $\phi = p/\rho_r$ is the geopotential perturbation, $p$ is the perturbation pressure and $\rho_r$ is a constant reference density. Still in Eqs. (6) $u_g = -\partial_y\phi/f$ and $v_g = \partial_x\phi/f$ are the geostrophic components of the wind perturbation. From the system of Eqs. (6), we form the linearized budget of the PV disturbance $q$. For this, we calculate $[\nabla \wedge ((6a),(6b),(6c))]\,.\nabla\Theta_b + \Lambda\partial_y(6d) - \theta_{0z}R_i^{-1}\partial_x(6b)$, and use Eq. (5), which yields :

$$(\partial_t + \mathbf{U}\nabla)\, \rho_r q + \nabla.\mathbf{J}_N = 0 \ , \quad \text{where} \tag{7}$$

$$
\begin{aligned}
\rho_r\, q(\mathbf{x}, z, t) &= \theta_{0z}\left((1 - Ri^{-1})\,\partial_x v_g - \partial_y u_g\right) + \Lambda\,\partial_y\theta + \Theta_y\,\partial_z u_g + f\partial_z\theta \ , \quad \text{and} &\text{(8)}\\
\mathbf{J}_N &= -\theta_{0z}\,(1 - Ri^{-1})\,\mathcal{G}\,\mathbf{e}_x + \theta_{0z}\,\mathcal{F}\,\mathbf{e}_y - \Theta_y\,\mathcal{F}\,\mathbf{e}_z \ . &\text{(9)}
\end{aligned}
$$

In Eqs. (7) and (9), $\mathbf{J}_N$ is the non-advective PV flux, and $R_i = \frac{N^2}{\Lambda^2}$ is the background flow Richardson number. Note that Eqs.(7)-(8)-(9) are the linearized version of Hoskins (1975) SG PV budget, with $\mathcal{F}$ added. Notably, $\mathbf{J}_N$ is everywhere parallel to the background isentropes ($\mathbf{J}_N.\nabla\Theta_b = 0$). And since these isentropes are advected by the background

4

flow, the global PV flux $\rho_r\, q\, \mathbf{U}(z) + \mathbf{J}_N$ never crosses them, which is consistent with the "PV impermeability theorem" (Haynes and McIntyre, 1987).

Then, to determine the surface response from the PV, we also consider the two linearized free-slip adiabatic boundary conditions:

$$(\partial_t + \mathbf{U}(0)\nabla)\,\theta + v\,\Theta_y \;=\; -\theta_{0z}\,\mathbf{U}(0)\nabla\mathcal{H} \ \ \text{at } z = 0 , \tag{10}$$

$$(\partial_t + \mathbf{U}(D)\nabla)\,\theta + v\,\Theta_y \;=\; 0 \ \text{at } z = D . \tag{11}$$

## 2.2   Inversion of the PV perturbation

If the forcings $\mathcal{F}$, $\mathcal{G}$, and $\mathcal{H}$ are specified, it is convenient to solve the Eqs. (7)–(11) in the Fourier space[1]. In this space, the PV perturbation in Eq. (7) is then

$$\rho_r\,\hat{q} = i\frac{1 - e^{i(\mathbf{k}.\mathbf{U}).t}}{\mathbf{k}.\mathbf{U}}\left\{\Theta_y\partial_z\hat{\mathcal{F}} + \theta_{0z}\left(-ik(1 - Ri^{-1})\hat{\mathcal{G}} + il\hat{\mathcal{F}}\right)\right\} , \tag{12}$$

provided that $\hat{q}(t = 0) = 0$. Introducing the geostrophic balance and the hydrostatic relation Eq. (6c), we can invert the PV in terms of geopotential via the elliptic equation :

$$\frac{\partial^2\hat{\phi}}{\partial z^2} - 2i\lambda_i\frac{\partial\hat{\phi}}{\partial z} - \left(\lambda_r^2 + \lambda_i^2\right)\hat{\phi} = \frac{g}{f\theta_r}\,\rho_r\,\hat{q} \ \ , \text{where} \tag{13}$$

$$\lambda_r = \frac{N}{f}\,\sqrt{1 - Ri^{-1}}\,|\mathbf{k}| \quad \text{and} \quad \lambda_i = l\frac{\Lambda}{f}. \tag{14}$$

First, we form a particular solution that contains the whole PV $\hat{q}$ and vanishes at $z = 0$ :

$$\hat{\phi}_p(\mathbf{k}, z, t) = e^{-\lambda z}\int_0^z e^{2\lambda_r z'}\int_{z'}^D -\frac{g\rho_r}{f\theta_r}\hat{q}\,e^{-\lambda^* z''}dz''dz' \ , \text{where} \tag{15}$$

$$\lambda = \lambda_r - i\lambda_i \ \text{and} \ \lambda^* = \lambda_r + i\lambda_i . \tag{16}$$

Then, to satisfy the boundary conditions, we add to this particular solution two boundary waves:

$$\hat{\phi}(\mathbf{k}, z, t) = \hat{\phi}_p(\mathbf{k}, z, t) + \hat{\phi}_u(\mathbf{k}, t)\,e^{-\lambda z} + \hat{\phi}_d(\mathbf{k}, t)\,e^{+\lambda^*(z - D)} . \tag{17}$$

In this formalism, the boundary conditions Eqs. (10)-(11) become

$$\lambda_r\,(\partial_t - i\mathbf{k}.\mathbf{U}(0))\left(\hat{\phi}_u - \hat{\phi}_d\,e^{-\lambda^* D}\right) - ik\Lambda\left(\hat{\phi}_u + \hat{\phi}_d\,e^{-\lambda^* D}\right) =$$

$$\left\{(\partial_t - i\mathbf{k}.\mathbf{U}(0))\,\partial_z\hat{\phi}_p(0) + \Lambda\hat{\mathcal{F}}(0)\right\}_W - \left\{i\mathbf{k}.\mathbf{U}(0)\,N^2(1 - Ri^{-1})\,\hat{\mathcal{H}}(\mathbf{k})\right\}_E \tag{18}$$

$$\lambda_r\,(\partial_t - i\mathbf{k}.\mathbf{U}(D))\left(\hat{\phi}_u\,e^{-\lambda D} - \hat{\phi}_d\right) - ik\Lambda\left(\hat{\phi}_u\,e^{-\lambda D} + \hat{\phi}_d\right) =$$

$$\left\{-\lambda_r(\partial_t - i\mathbf{k}.\mathbf{U}(D))\,\hat{\phi}_p(D) + ik\Lambda\,\hat{\phi}_p(D) + \Lambda\hat{\mathcal{F}}(D)\right\}_W , \tag{19}$$

at $z = 0$ and $z = D$ respectively. In the right hand of Eqs.(18)–(19) we have separated the forcings due to the GWs $(W)$, and to the enveloppe $\mathcal{H}$ $(E)$. In the following, the response is always described at the ground, where $\hat{\phi} = \hat{\phi}_W + \hat{\phi}_E$ because $\hat{\phi}_p(z = 0) = 0$.

[1] convention : $\phi(\mathbf{x}) = \int_{-\infty}^{\infty}\int_{-\infty}^{\infty}\hat{\phi}(\mathbf{k})e^{-i\mathbf{k}\mathbf{x}}dkdl$, where $\hat{\phi}(\mathbf{k}) = \frac{1}{4\pi^2}\int_{-\infty}^{\infty}\int_{-\infty}^{\infty}\phi(\mathbf{x})e^{i\mathbf{k}\mathbf{x}}dxdy$.

## 2.3 Evaluation of $\mathcal{F}(\mathbf{x}, z)$

To evaluate the force $\mathcal{F}(\mathbf{x}, z)$, we first calculate a net force $\overline{\mathcal{F}}(z)$ using the linear theory of GWs in a linear background shear flow (Shutts 1995, and Appendix):

$$\overline{\mathcal{F}}(z) = -\frac{d}{dz}\,\overline{\mathbf{u}'\,w'}, \text{ where } \overline{\mathbf{u}'w'} \equiv \frac{1}{\pi L^2} \int_{-\infty}^{+\infty} \int_{-\infty}^{+\infty} \mathbf{u}'\,w'\,dxdy \,. \tag{20}$$

In Eq. (20), $\mathbf{u}'$ and $w'$ are the small-scale velocities associated with $h'$. Then, we consider that the horizontal distribution of $\mathcal{F}(\mathbf{x}, z)$ resembles the enveloppe profile $\mathcal{H}(\mathbf{x})$:

$$\mathcal{F}(\mathbf{x}, z) = \overline{\mathcal{F}}(z)\, e^{-\frac{x^2+y^2}{L^2}} \,. \tag{21}$$

Although in Eq. (21), $\mathcal{F}(\mathbf{x}, z)$ results in a net force equal to $\overline{\mathcal{F}}(z)$, Eq. (21) assumes that the GWs field stays confined over the mountain range $\mathcal{H}$. This assumption is only valid for hydrostatic waves in the absence of shear, while for the background flow we consider here, Shutts and Gadian (1999) have shown for an isolated mountain that the GWs field is spread downstream over a distance that can reach few times the horizontal scale of the mountain. Nevertheless, we adopt this assumption for several reasons. First, the drag $\overline{\mathbf{u}'w'}$ is less widely spread because it is quadratic. Second, Lott (2003) have shown in 2D that the spread of the drag is reduced if we increase the vertical resolution and add a small amount of dissipation to take account of the breaking. Third, since we consider here the combined effect of several different anisotropic individual ridges, a possible local shift of the force over a distance comparable to $2\pi/|\mathbf{k}_w|$ can be reasonably neglected in respect to $L$, the scale of the global mountain.

As our GWs have horizontal wavenumber $\mathbf{k} \sim \pm\mathbf{k}_w$ (Eq. (1) and Figs. 1b,c), the forcing $\mathcal{F}$ is only significant if there exists a critical level $z_w$ for $\mathbf{k}_w : \mathbf{U}(z_w).\mathbf{k}_w = 0$. In other words, the background wind has to pass from one side of the ridges to the other when $z$ increases (Fig. 1b). For a cold front in the Northern Hemisphere, e.g. $V_0 < 0$ and $\Lambda > 0$, this only occurs if $k_w.l_w > 0$ (Fig. 1b,c). For a warm front ($V_0 > 0$ and $\Lambda > 0$) this only occurs if $k_w.l_w < 0$. In both cases, the total force is well approximated by

$$\overline{\mathcal{F}}(z) \approx \frac{1}{2\sqrt{\pi}}\, N\Lambda L H_0^2\, k_0(z)^2\, e^{-L^2\|\mathbf{k}_w\|^2 + L'^2 k_0^2}\, \frac{\Lambda z |V_0|}{\|\mathbf{U}(z)\|^2}\, \left(\mathbf{e}_x - \frac{U(z)}{V_0}\mathbf{e}_y\right) \tag{22}$$

$$\text{where: } k_0 = \left(k_w - l_w \frac{U(z)}{V_0}\right) \Big/ \left(1 + \frac{U(z)^2}{V_0^2}\right) \,, \text{ and } L'^2 = \left(1 + \frac{U(z)^2}{V_0^2}\right) L^2 \,. \tag{23}$$

Coherently, $\mathcal{F}(z)$ is everywhere orthogonal to the background flow $\mathbf{U}(z)$ (see Appendix).

## 2.4 Computation

To solve this problem numerically, we consider a horizontally periodic domain of size 20000km×20000km×10km. The fields are represented by $512 \times 512$ harmonics and 81 vertical levels, yielding a resolution of 40km×40km×125m. First, we compute analytically the PV anomaly using the diagnostic Eq. (12), and integrate it vertically by a trapezoïdal approximation to evaluate $\hat{\phi}_p$ in Eq. (15). Then, we solve the first order differential Eqs. (18)-(19), treating separately the parts "W" and "E". This yields temporal integrals that converge for a time step of *2 hours (hrs)*.

## 3 Cold front with no tropopause

In this section, we place the tropopause altitude at $D = \infty$. And we consider an idealized cold front moving toward the South in the Northern Hemisphere midlatitudes, across an

idealized mountain range. The flow and orography parameters are respectively :

$$\theta_r = 300 \text{ K}, \ \rho_r = 1 \text{ kg m}^{-3}, \ f = 10^{-4} \text{ s}^{-1} \ , \ N = 10^{-2} \text{ s}^{-1} \ ,$$
$$\Lambda = 4.10^{-3} \text{ s}^{-1} \ , \ U_0 = 0 \text{ ms}^{-1} \ , \ V_0 = -20 \text{ ms}^{-1}. \tag{24}$$

$$H_0 = 800 \text{ m} \ , \ L = 200 \text{ km} \ , \ |\mathbf{k}_W| = \frac{2\pi}{70000} \text{ m}^{-1}, \text{ with } k_w = l_w. \tag{25}$$

The mountain range half-height width is $2L * \sqrt{\ln 2} \approx 330\text{km}$. It is typically constituted of 5 to 7 ridges, which are 70km wide and oriented South East - North West (Fig.1b). The dimensionless mountain heights $\frac{NH_0}{fL} = 0.4 < 1$ for the large scale orography $\mathcal{H}$, and $\frac{N2H_0}{V_0} = 0.8 < 1$ for the small scale orography $h'$, justify a linear treatment for both. The large scale Rossby number is $\frac{V_0}{fL} \sim 1$, and the ratio between the large and the short scales is $2L|\mathbf{k}_w|/2\pi \sim 6 > 1$. Note that we could arbitrarily choose to have a bigger number of thinner ridges in the same enveloppe as here. But therefore, we should have also reduced the height of these ridges, to conserve a reasonable orographic variance and force.

## 3.1   PV anomaly due to the absorbed GWs forcing $\mathcal{F}$

The vertical profile of the net force $\overline{\mathcal{F}}(z)$ in Eq. (22) is displayed in Fig. 2. Each component reaches a maximum near $z_w = 5km$, and is only substantial over a vertical depth of 1 or 2 km around $z_w$. In the rest of the paper we will refer to this area as the critical zone.

The Figs. 3a,b,c show three horizontal sections of the PV anomaly due to $\mathcal{F}$ in the critical zone at t=12hrs. At the three levels, the PV amplitude is between 0.4-0.8 PVU, and the PV patterns are predominantly oriented in the direction of the background wind $\mathbf{U}(z_w)$. This general orientation follows that once produced by $\mathcal{F}$ aloft the mountain, the PV is advected by the background flow. To interpret the differences between those three levels, one visualizes schematically the non advective PV flux $\mathbf{J}_N$ in Fig. 4. The Fig. 4a shows that $\mathbf{J}_N$ is pointing upward to be parallel to the isentropes. In the $(y, z)$ plane, $J_{Nz}$ essentially takes the PV from below $z_w$ to put it above (Fig. 4a), yielding the predominantly positive PV lobe above $z_w$ (Fig. 3a) and the predominantly negative one below (Fig. 3c). Near the altitude $z_w$, the divergence of the vertical component of the non-advective PV flux is null,

$$\partial_z J_{Nz} = \Theta_y \partial_z \mathcal{F} = 0 \ , \tag{26}$$

therefore the PV is only due to the vector $\mathbf{J}_{Nxy} = J_{Nx} \mathbf{e}_x + J_{Ny} \mathbf{e}_y$, which is nearly opposite to the wind, the force $\mathcal{F}(z_w)$ being perpendicular to it (Fig. 4b). Hence, near $z_w$, $\mathbf{J}_{Nxy}$ tends to take PV from downstream to put it upstream, according to the direction of $\mathbf{U}(z_w)$. At small times, it results in a positive PV anomaly along the upstream flank of the mountain and a negative one downstream (Fig. 4b). Afterwards, the negative PV anomaly produced aloft the mountain is advected downstream at the velocity $\mathbf{U}(z_w)$, yielding the mid-tropospheric start-up anticyclone in Fig. (3b). Still near $z_w$ but over the mountain, the long-term response is a steady-state cyclonic PV anomaly (Fig. (3b). There, the PV due to $\mathbf{J}_{Nxy}$ is exactly balanced by the advection term,

$$(\mathbf{U}.\nabla) \rho_r q + \nabla.\mathbf{J}_{Nxy} = 0 \ . \tag{27}$$

The PV structure in Fig. 3 essentially represents a PV banner, whose characteristic horizontal width and depth are fixed by the width and depth of the critical zone, around $2L = 400\text{km}$ and 2km respectively (see Fig. 2 and 4), while its length is controlled by the advection (i.e. around $|\mathbf{U}(z_w)|.t$). This PV banner has a 3D structure that is very different from the PV banners occurring in barotropic flows when the low level flow passes around

individual mountain peaks or when mountain GWs break in the absence of critical levels. In these cases, the effect of the mountain can still be modeled by a non-advective PV flux $\mathbf{J}_N$. It is nevertheless perpendicular to the background wind rather than parallel to it, resulting in PV lobes of opposite signs localized one next to the other in the horizontal (Schär and Durran, 1997).

## 3.2  Surface pressure $\phi_W$ due to the forcing $\mathcal{F}$

The Figs. 5a,b,c show the surface pressure perturbation induced by the GWs momentum deposit. At small time (Fig. 5a), it presents a small amplitude (approx. -0.1mb) trough over the mountain and a ridge downstream of it (towards $\mathbf{U}(z_w)$), its amplitude is around 0.2mb. In a longer term (Figs. 5b,c), the trough over the mountain near disappears, while the downstream ridge extends along the direction of $\mathbf{U}(z_w)$. To the west of this extending ridge, a second trough is developing (Figs. 5b,c). At 36hrs, the maximum amplitude of the surface signal is 1.1mb.

To interpret this response, Fig. 6 shows the surface temperature anomaly $\frac{\theta_r}{g} \partial_z \phi_p(0)$ associated with the particular solution $\phi_p$. This term is central because it translates the PV into Eady waves forcing (see Eq. (18)) via the weighted average (in the Fourier space):

$$\frac{\theta_r}{g} \partial_z \hat{\phi}_p(\mathbf{k}, z = 0, t) = -\int_0^D \frac{\hat{q}}{f} e^{-\lambda^* z} dz . \tag{28}$$

At t=12hrs, $\frac{\theta_r}{g} \partial_z \phi_p(0)$ is negative over the mountain, and positive downstream of it. This follows that the mid-troposphere PV in Fig. (3) is predominantly positive over the mountain and negative downstream of it. Note also that the positive lobe in surface temperature exceeds in amplitude the negative one, because the negative PV in Fig. (3)c has a stronger influence at the surface than the positive one in Fig. (3)a. Note also that the pattern of $\frac{\theta_r}{g} \partial_z \phi_p(0)$ is substantially larger in horizontal size than the PV pattern. Again, this is due the weight $e^{-\lambda_r z}$ in Eq. (28), which favors the large scales, a general property of PV inversion operators (Hoskins et al, 1985). Still at t=12hrs, the surface trough over the mountain and the downstream ridge in Fig. 5a are essentially needed for the surface temperature $\frac{\theta_r}{g} \partial_z \phi_W(0)$ to oppose $\frac{\theta_r}{g} \partial_z \phi_p(0)$.

At later stages (t=24hrs, 36hrs), the temperature pattern $\frac{\theta_r}{g} \partial_z \phi_p(0)$ is more complex (Fig. 6b,c), with an elongated negative anomaly appearing along the North East flank of the extending downstream positive anomaly. This negative anomaly, is the surface signature of the upper level positive PV (the one shown in Fig. (3)a at t=12hrs). At these times, it is no longer masked by the lower level negative anomaly (the one in Fig. (3)c at t=12hrs), because the wind is turning clockwise with altitude.

As a result, the surface response $\phi_W$ is predominantly anticyclonic near along the axis of $\mathbf{U}(z_w)$ (Figs. 5b,c). Nevertheless, it presents a trough along the South-Eastern flank of this ridge: to the opposite of the place where the elongated negative surface anomaly of $\frac{\theta_r}{g} \partial_z \phi_p(0)$ is located in Figs. 6b,c. This witnesses of the fact that boundary Eady waves start to modulate the surface response via the meridional thermal advection in Eq. (18), and make it differ from the simple mirror image of the PV deposit.

To support this last statement, we note that the Eady waves forcing $\frac{\theta_r}{g} \partial_z \phi_p(0)$ (Fig. 6) has a quite stationary structure upstream of the advected start-up anticyclone. In terms of Eady waves dispersion relationships, this translates into:

$$\omega = \mathbf{k}.\mathbf{U}(z = \frac{1}{\lambda_r}) = k \frac{\Lambda}{\lambda_r} + l V_0 = 0 . \tag{29}$$

As the shape of $\frac{\theta_r}{g} \partial_z \phi_p(0)$ also imposes $k \sim l$, Eq. (29) yields $\lambda_r \sim \frac{\Lambda}{-V_0} = 2.10^{-4}\,\mathrm{m}^{-1}$, and a dominant wavelength $\frac{2\pi}{|\mathbf{k}|} \sim 3000\,\mathrm{km}$ rather consistent with the Fig. 5c. For these

scales, the group velocity points towards the South-South-West:

$$\mathbf{C_g} = \left( \frac{\Lambda}{\lambda_r} \frac{l^2}{|\mathbf{k}|^2} , \frac{\Lambda}{\lambda_r} \frac{l^2}{|\mathbf{k}|^2} \right) \sim \left( -\frac{V_0}{2} , \frac{3V_0}{2} \right) , \tag{30}$$

whereas $\mathbf{U}(z_w)$ is South-West. Accordingly, we observe the development of a trough at the West of the extending ridge.

### 3.3  Surface pressure $\phi_E$ due to $\mathcal{H}(\mathbf{x})$

The time evolution of $\phi_E$ is shown in Figs. 5d,e, and f at=12hrs, 24hrs, and 36hrs respectively. A boundary Eady lee wave is developing and extending downwind according to $\mathbf{U}(0) = V_0 \, \mathbf{e}_y$. The wave is bounded downstream by the start-up cyclone due to the warm potential temperature anomaly $\theta_{0z} \, \mathcal{H}$ present over the mountain range when $t < 0$ and swept away by $\mathbf{U}(0)$ when $t > 0$. It is bounded over the mountain by an anticyclonic pattern due to vortex compression. The corresponding high keeps almost constant after 12hrs and reaches 1.2 mb at 36hrs. Immediately downstream of the mountain a trough is settling, whose amplitude reaches -1.3mb at 36hrs. The amplitudes obtained are significantly smaller than in Smith (1984, 1986) because our mountain is substantially smaller in width and height.

As in Section 3.2 this surface response can also be interpreted in terms of stationary boundary Eady waves dynamics. In this case the large scale orography induces a steady forcing with dominant wavenumbers $|\mathbf{k}| \approx 1/L$, and Eq. (29) implies

$$l/k = -\Lambda/(\lambda_r V_0) \sim 0.5 > 0 \ . \tag{31}$$

Accordingly, the troughs and ridges are oriented from North-West to South-East, and are strongly inclined along the $y$ axis. Likewise, Eq. (31) permits to predict $2\pi/l \approx 4\pi L = 2400$km, which roughly corresponds to the crest-to-crest distance along the y-axis in Fig. 5f. These values yield a dominant group velocity consistent with the Eady lee wave extension along the $y$-axis in Fig. 5f:

$$\mathbf{C_g} \approx (6 \ ; -20) \ \mathrm{ms}^{-1} \ . \tag{32}$$

### 3.4  Total response at the surface $\phi = \phi_W + \phi_E$

The total response $\phi = \phi_W + \phi_E$ is displayed in the Figs. 5g,h,i. Although the GWs effect is rather small, they reduce by near 20% the ridge produced by the large-scale orography over the mountain, as well as the downstream trough. More pronounced effects occur further downstream. In particular the ridge produced by the GWs and which extent below the PV banner in Figs. 5b, affects substantially the surface response in the far field.

## 4  Warm front with no tropopause

In this part, we consider the case of a warm front by taking $V_0 = 20 \ ms^{-1}$ in our model. To obtain a significant force $\mathcal{F}$ we also rotate the small-scale ridges and take $k_w = -l_w$ (see Appendix). All the other parameters are the same as in Section 3.

As in the cold front case, the PV anomaly on both flanks of the critical zone has an elongated structure. It is predominantly positive above $z_w$ and negative below (Figs.7a,c). This is almost as in the cold front case in Fig. 3a,c. Near the altitude $z_w$ nevertheless (Fig. 7b), the PV anomaly over the mountain is negative, and an opposing pattern of positive PV is advected downstream at the velocity $\mathbf{U}(z_w)$: the opposite to what occurs in the cold front case in Fig. 3b.

This last difference between the cold front case and the warm front case is an important result that has a simple dynamical origin. The necessity that there exist critical levels in the troposphere for the GWs to affect the large scale flow, imposes that the GWs force has one component in the direction of the shear $\Lambda$ (the x-component in our case, see Fig. 4b). Its other component is opposed to the low level wind, which is natural for a gravity wave drag. Where this force acts, $\mathcal{F}$ makes an angle with $\mathbf{U}(z_w)$ equal to $\pi/2$ in the cold front case, and equal to $-\pi/2$ in the warm front case. From this, it follows that the horizontal component of the PV flux $\mathbf{J}_{Nxy}$ is such that $\mathbf{J}_{Nxy}.\mathbf{U}(z_w) < 0$ in the cold front case, whereas $\mathbf{J}_{Nxy}.\mathbf{U}(z_w) > 0$ in the warm front case. Because of this difference, the surface response to the GWs in the warm front case (Figs. 8a,b,c) presents no symmetry with that in the cold front case (Figs. 5a,b,c). On the other hand, the response to the large-scale orography $\phi_E$ is the symmetric of the cold front response, in respect to the x-axis (Figs. 8d,e,f and Figs. 5d,e,f).

In response to the PV pattern in Fig. 7, the surface response $\phi_W$ is dominated by a strong anticyclonic lobe which keeps attached to the mountain (Figs. 8a,b,c). Immediately downstream according to $\mathbf{U}(0)$ a substantial trough develops. Note also that the magnitude of the response is stronger than in the cold front case (between 1.8 mb and -1.2 mb at t=36hrs). It follows that the anticyclonic PV anomalies over the mountain and extending below $z_w$ downstream of it in Figs. 7b, and c reinforce each other to produce a strong surface response near the mountain. By summing the two responses, it is apparent in Figs. 8g,h,i that in this case the absorbed GWs reinforce the anticyclone over the mountain as well as the downslope trough.

# 5    Sensitivity experiments
## 5.1    Quasi-Geostrophic simulations

The fundamental reason for choosing the SG formalism rather than the QG formalism is that we obtain a more accurate PV budget, closer to the primitive equations PV budget. More precisely, in our case, the non-advective PV flux $\mathbf{J_N}$ has a vertical component $J_{Nz}$ that keeps $\mathbf{J}$ parallel to the tilted isentropes (Haynes and McIntyre, 1987). This vertical component is neglected in the QG formalism. To evaluate its significance, we have repeated the cold and warm front experiments in Sections 3 and 4 using a QG version of the model of section 2. To do it, we take $\Theta_y \mathcal{F}_z = Ri^{-1} = 0$ in the PV Eq. (12) and $Ri^{-1} = \lambda_i = 0$ in the definition of the vertical decay length $\lambda$ Eq. (14).

The most noticeable difference is that the warm front response is exactly anti-symmetric with the cold front response according to the x-axis (Fig. 9). Because of the neglect of $J_{Nz}$, at all altitudes the PV is due to an horizontal flux $\mathbf{J}_{Nxy}$ that is aligned with the wind (not shown), so it resembles that at $z_w$ in the SG simulations (Fig. 3b and 7b). The QG simulations fail in simulating the substantial, sign definite, and elongated PV anomaly located on the lower flank of the critical zone (Fig. 3c and 7c). That is the reason why the surface signal in the QG cases is much smaller than in the corresponding SG cases.

Nevertheless, we can notice that downstream of the mountain the GWs remain cyclolitic for a cold front case and cyclogenetic for a warm front. Over the mountain, the GWs still produce a low for the cold front case and a high for the warm front.

## 5.2    Front, orography and critical zone altitude

The numerical simplicity of our model permits to analyze many different flow and orography configurations. For example, increasing only $H_0$ favors the GWs forcing (varying in $H_0^2$, Eq. (22)) relatively to the large scale orography forcing (in $H_0$, Eq. (18)). Increasing the number of ridges in our mountain (i.e. increasing $|\mathbf{k}_w|L$) results in the same effect, even if $L$ is fixed, and although the critical zone becomes thinner. Changing the orientation of the ridges (i.e. the angle $\widehat{(\mathbf{e}_x; \mathbf{k}_w)}$) has a more subtle effect. In the cold front

case, for $0 < \widehat{(\mathbf{e}_x; \mathbf{k}_w)} < \frac{\pi}{4}$, the GWs meet critical levels nearer the ground. It results in 3 effects : (i) the PV anomaly is nearer the ground, (ii) the advection of PV is slower, and (iii) the axis of the PV anomaly is closer to the surface wind $V_0\,\mathbf{e}_y$. As illustrated in Figs. 10a,b,c, this makes the surface response (i) thinner in width, (ii) shorter in length, and (iii) oriented closer to the surface wind $V_0\,\mathbf{e}_y$. The same results hold for the warm front case and for $-\frac{\pi}{4} < \widehat{(\mathbf{e}_x; \mathbf{k}_w)} < 0$ (not shown). The compromise of those different processes is summarized in Fig. 11, where the extrema of $\phi_W$ at t=36hrs are plotted versus $\widehat{(\mathbf{e}_x; \mathbf{k}_w)}$ in the cold and warm front cases. Notably, in both cases, the maximum amplitude is obtained for an intermediate value of $|\widehat{(\mathbf{e}_x; \mathbf{k}_w)}|$, and not for $|\widehat{(\mathbf{e}_x; \mathbf{k}_w)}| \approx 0$ for which $z_w$ is nearer the ground. The reason is that $z_w \approx 0$ requires $\mathbf{k}_w.\mathbf{U}_0 \approx 0$, that is a quasi null cross-ridge velocity, and therefore a weak GW drag (see Eq. (41) in Appendix). The amplifying effect of the descent of the critical zone by decreasing $|\widehat{(\mathbf{e}_x; \mathbf{k}_w)}|$ is thus balanced by a decrease of the total force amplitude.

## 5.3 Influence of the tropopause

To study the impact of the geostrophic baroclinic instability on our results, we place a rigid lid at the altitude $D = 10\,km$. A conventional linear stability analysis for our model shows that unstable baroclinic modes have wavelengthes exceeding $2\pi/(2.6*f/ND) \sim 2400\,km$, and that the most unstable mode is oriented in the along-front direction ($\mathbf{\Lambda} = \Lambda\mathbf{e}_x$) with a wavelength near $3700\,km$ ($\mathbf{k} = 1.7*f/(ND)\,\mathbf{e}_x$).

As shown in the Figs. 12a,b,c for the cold front case in Section 3, in the short term (12hrs, Fig. 12a) the instability essentially has a slight quantitative effect on the surface pressure pattern, compared to the case with no tropopause in Fig.5a. At t=24hrs (Fig. 12b), the presence of long unstable modes starts to modulate the response substantially. In particular, near and over the mountain the trough is more intense (see Fig.5b), and its horizontal scale exceeds $2000\,km$ along $\mathbf{\Lambda}$. Later (t=36hrs, Fig. 12c), the long modes influence is even stronger. Nevertheless, they do not affect much the maximum amplitude of the signal, but rather spread it towards $\mathbf{\Lambda}$. A qualitatively comparable behavior occurs in the warm front case of Section 4 (Figs. 12d,e,f), except that it is quantitatively less pronounced.

# 6 Extension to more realistic mountains

The near monochromatic nature of the small scale orography used until now results in a rather thin critical zone. In reality however, mountains have broad band spectra and the GWs can interact with critical levels almost everywhere over the entire troposphere depth. To account for this, we follow Gregory et al. (1998) and represent the real orography spectrum over square domains of size $X * Y$ by a spectral density function $A(\mathbf{k})$ which captures exactly the orographic variance:

$$\frac{1}{XY} \int_0^X \int_0^Y h'^2 dx dy = \int_0^{+\infty} \int_0^{2\pi} \frac{4\pi^2}{XY} |\hat{h}(K, \alpha)|^2 \, K dK d\alpha = \int_0^{+\infty} \int_0^{2\pi} A(K, \alpha) \, K dK d\alpha . \quad (33)$$

In Eq. (33) $K$ and $\alpha$ are the polar coordinates of $\mathbf{k}$. $\hat{h}(K, \alpha)$ is the Fourier transform of $h'$ inside of the domain $X * Y$, that can be estimated for real data by the FFT coefficient $\tilde{h}$ calculated from the discrete series of $h'$. We then assume an isotropic spectral density in the wavenumber band relevant for gravity waves:

$$K A(\mathbf{k}) = a \left(\frac{K_0}{K}\right)^\gamma , \text{ for } K_L < \|\mathbf{k}\| < K_U . \quad (34)$$

In Eq. (34) $K_0$ and $\gamma$ are constants that vary regionally, and $a = 1m^3$ is introduced for dimension consistency. We take $K_U = 2\pi/(10\,\text{km}) \approx N/V_0$ because disturbances with

shorter wavelength do not propagate vertically, and $K_L = 2\pi/\sqrt{X^2 + Y^2}$, i.e. approximately the longest harmonic the domain $X * Y$ can represent. Note that we could have defined $K_L$ as the lower cut-off of the stationnary inertia-GWs, $K_L = f/V_0 \approx 1200$km. This is larger than the size of our domain, hence not represented in our spectrum analysis. Nevertheless, we have checked that the following analyses are not sensitive to $K_L$: for such low values of $\gamma$, the orographic variance concentrates on the small scales.

To evaluate the effect of this spectrum in the context of our model, we consider the effect of the small-scale mountains located in a domain of size $\pi L^2 = XY$, and use the method in Appendix to evaluate the net force due to $A(\mathbf{k})$:

$$\overline{\mathcal{F}} = \frac{2N\Lambda a}{2 - \gamma} \left[ \left(\frac{K_0}{K_U}\right)^\gamma K_U^2 - \left(\frac{K_0}{K_L}\right)^\gamma K_L^2 \right] \frac{\Lambda z |V_0|^3}{||\mathbf{U}(z)||^4} \left( \mathbf{e}_x - \frac{U(z)}{V_0} \mathbf{e}_y \right). \tag{35}$$

We then distribute this force regionally as in Section 2: $\mathcal{F}(\mathbf{x}, z) = \overline{\mathcal{F}}(z) e^{-\frac{x^2 + y^2}{L^2}}$.

To give realistic values to the parameters $K_0$ and $\gamma$, we have considered the Alpine sector (5°E-16°E; 43°N-48°N) and used the ETOPO2 dataset[2]. In this sector, we define 30 partially overlapping square domains, each of size $XY = 352$km$^2 = \pi L^2$, giving $L = 200$km as in Section 3,4,5 (Fig. 13a). For each of these domains, we estimate $(\gamma, \ln(K_0^\gamma))$ by a best square fit between $A(\mathbf{k})$ and the azimuthal mean of the orography periodogram $\tilde{h}\tilde{h}^*$. An example for one particular box [5°26'E, 9°58'E] × [43°48'N, 46°58'N] is shown in Fig. 13. For this box, the best fit is $\gamma = 0.96$ and $\ln(K_0^\gamma) = 10.2$ (Fig. 13b). For other boxes, the results are summarized in Fig. 13c: even if the parameters $\gamma$ and $\ln(K_0^\gamma)$ have significant variations (the range obtained for $\gamma$ is from 0.56 to 1.02), the resulting force for each box has a rather stable magnitude around $2\,10^{-4}\,\mathrm{kg\,m^{-2}\,s^{-2}}$. Therefore, in our simulations we can use, for the force, the mean values:

$$\gamma = 0.76 \;;\; \ln(K_0^\gamma) = 13.5 \;. \tag{36}$$

Note that our $\gamma$ is smaller than in Gregory et al. 1998 (who found $\gamma > 1$), probably because the Alps are sharper than the mountains studied by these authors.

The Figs. 14a,b present the vertical profiles of $\mathcal{F}$ obtained with Eqs. (35)-(36) and for the cold front of Section 3. As expected, the critical zone is deeper than in Fig. 2 and covers the entire troposphere. The surface response to this force in the absence of tropopause is shown in Fig. 14c at t=36hrs. It resembles very much that of the idealized case in Fig.5c. A predominant ridge is followed by a weaker trough, both being embedded in the South to South-East sector. The dominant wave-vector is very similar to that of Subsection 3.2, although not so well defined. The reason is that the critical zone is deep, giving no precise horizontal axis to the PV pattern.

# 7 Discussion and Conclusion

This paper gives an heuristic evaluation of the significance of mountain GWs for the synoptic-scale dynamics near large mountain ranges, in the presence of directional critical levels. The model used is an extension of the model of Smith (1984) for lee cyclogenesis. It includes a representation of the GWs adapted from Shutts (1995). The interaction between the GWs and the large-scale flow occurs via the PV anomaly, which is produced by the force due to the GWs which encounter critical levels in the troposphere.

Section 3 details this interaction for a cold front, in the case where there is a good separation between the small-scale dynamics and the large-scale dynamics. In a configuration such that almost all the GWs encounter critical levels, they induce a force in a

---

[2]around 2 km horizontal resolution, see the NGDC's web-site: www.ngdc.noaa.gov/mgg/fliers/01mgg04.html

thin critical zone centered around a well defined altitude $z_w$. The level $z_w$ depends on the configuration of the front relatively to the orientation of the anisotropic small-scale orography. This force is everywhere perpendicular to the background flow and produces a PV anomaly around $z_w$ that is advected and steered by the background wind. Near $z_w$, the PV anomaly is predominantly cyclonic aloft the mountain, and it presents a start-up anticyclone that travels at the velocity $\mathbf{U}(z_w)$ away from the mountain (Fig. 3). Below $z_w$ the PV anomaly is predominantly anticyclonic, whereas above $z_w$ it is predominantly cyclonic. Accordingly the surface response presents at small time (12hrs in Fig. 5a) a trough over the mountain and a ridge downstream. In a longer term, this response is modulated by Eady waves (Figs 5b, and c): the trough over the mountain becomes quite small, and an elongated ridge builds-up immediately downstream towards $\mathbf{U}(z_w)$. The GWs thus tend to slightly reduce the amplitude of the response to the large-scale orography, notably the ridge over the mountain and the lee trough (Figs. 5d,e,f). As the lee trough is associated with lee-cyclone initiation in Smith (1984), we can argue that the GWs are cyclolytic in the cold front case.

In Section 4 we repeat the same study in the warm front case (Figs. 7–8), after rotating by $90^o$ the orientation of the mountain ridges in order that the GWs exert a substantial force. In this case, the PV anomaly produced by the GWs is predominantly anticyclonic over the mountain and cyclonic downstream (Fig. 7). It is also predominantly anticyclonic below $z_w$ and cyclonic above. Hence, the surface response presents a large-scale ridge attached to the mountain (Figs. 8a,b,c), and extending below the PV anomaly, toward $\mathbf{U}(z_w)$ (Fig. 7). Eady waves dynamics produce a trough downstream of the mountain, toward the surface wind $\mathbf{U}(0)$ (Figs. 8b,c). In this case, and contrary to the cold front case, the GWs reinforce the ridge over the mountain and the downstream trough (Figs. 8d,e,f).

The rest of the paper consists in doing tests of the robustness of these results. They indeed seem to be linked to geometrical properties of the GWs directional critical levels, indicating that they are rather systematic. In Section 5a, we adopt the QG framework. This illustrates the important role of the vertical component of the PV flux in baroclinic environments. In Section 5b, we change the orientation of $\mathbf{k}_w$, and other crucial parameters. Even if those changes have some quantitative effects on the amplitude or the horizontal scale of the surface response, the cyclolytic nature of the GWs in the cold front case stays unchanged. The same is true in the warm front case, where the interaction remains cyclogenetic. The introduction of a tropopause in Section 5c is more significant qualitatively, even if in our model, the baroclinic instabilities can only modulate the GWs response at horizontal scales much larger than discussed up to now. The effect is particularly pronounced in the cold front case (Figs. 12a, b, and c) where, compared to the same case without a tropopause (Figs. 5a, b, and c) the trough over the ridge becomes rather large in the long term (Fig. 12c) instead of becoming small (Fig. 5c), while the ridge downstream becomes rather small, instead of being large. In the warm front case (not shown) the effect of the GWs aloft the mountain and immediately downstream of it stays the same as without a tropopause. It is only in the far field and at large scales that the influence of the baroclinic instabilities become substantial.

In Section 6 we present an extension of our model to more realistic small-scale orographic spectra. We use for this a method presented in Gregory et al. (1998) in the context of the parameterization of mountain GWs via a spectral method in the UKMO model. This method consists again in evaluating the GWs force exactly, but using a realistic spectral density function for the orography. For the case of the Alps (Fig. 13), the GWs force is more broadly distributed over the troposphere. Nevertheless, the surface responses to the GWs (Figs 14) share many properties with the responses for the idealized orography profiles used in Sections 3, 4, and 5.

Despite the attractive simplicity of our model, these results should be interpreted with some caution. For instance, the neglect of unbalanced effect can be inaccurate for shears larger than here: the inertio-gravity waves generated during the interaction (Lott, 2003; Vadas et al, 2003) or the non-geostrophic unstable baroclinic modes (Plougonven et al, 2005) may have a substantial influence at the surface. More seriously, by representing the fronts by uniform shears we do not consider the barotropic growth of unstable modes that the smooth mountain and the GWs may trigger. This may result in effects rather different from those discussed here, in particular because the horizontal scale of the unstable modes may be much closer to the horizontal scale of the mountain.

Nevertheless, we believe that the structure of the PV anomalies we discuss here is of some interest. They are produced by PV fluxes that are everywhere parallel to the background wind, a situation rarely discussed in the literature. As a result, they do not resemble the horizontal PV banners that are often discussed. These PV anomalies are also strongly affected by the inclination of the isentropes. For these reasons, they may reflect some aspects of the mesoscale and synoptic scale PV patterns found in the observations. For example, Hoinka et al (2003) have carried out an analysis of the MAP IOP 15 (see also Buzzi et al., 2003) in which a PV streamer from the low stratosphere passes above the Alps, triggering lee cyclogenesis. They mention the importance of the breaking GWs in the cut-off process and the presence of enhanced shear. Since the order of magnitude of our PV anomalies is comparable to theirs, the process we have studied here might have some relevance in their case.

Another interest of this study is to give a theoretical approach to the problem of mountain GWs parameterization in large-scale models. In this respect, the fact that the response to the GWs is generally smaller than the response to the large-scale orography is reasonable. The SSO parameterizations are intended for correcting errors, not for producing the dominant signal. In this context, it gives two messages.
First, a rather systematic error of large-scale models is that they underestimate, at least in winter, the anticyclonic circulation that occurs over the large-scale mountains. These errors have been corrected in the past either by introducing an envelope orography, or by introducing lift forces oriented perpendicularly to the geostrophic flow and towards the right (in the Northern Hemisphere). The two approaches are in good part equivalent (Lott 1999). Although the GWs force is also perpendicular to the flow, our results show that it does not systematically help the building-up of anticyclones over mountains. Indeed, it is probably the other way round because cold fronts are stronger than warm fronts in a climatological sense. Second, our results show that absorbed GWs have little chance to help lee-cyclogenesis, and seem to have a rather cyclolytic influence, if we again assume that cold fronts are more frequent.

# APPENDIX
# Evaluation of the GWs force $\overline{\mathcal{F}}$

We use the linear Boussinesq theory of hydrostatic stationary mountain GWs in uniform background shears (Shutts, 1995). The vertical velocity for each monochromatic wave satisfies

$$\frac{\partial^2 \hat{w}'}{\partial z^2} + \frac{N^2}{(\mathbf{k}.\mathbf{U}(z))^2}\left(k^2 + l^2\right)\hat{w}' = 0 \ , \text{ with } \hat{w}'(0) = -i\mathbf{k}\mathbf{U}_0\,\hat{h}'. \tag{37}$$

The waves which present a critical level at $z_c = -\frac{\mathbf{k}\mathbf{U}_0}{k\Lambda} > 0$ can be written

$$\hat{w}'(z) = -i\mathbf{k}\mathbf{U}_0\,\hat{h}'\left(1 - \frac{z}{z_c}\right)^{1/2 + \epsilon\,i\alpha} \ , \epsilon = \pm 1 \ , \text{ for } z < z_c \tag{38}$$

$$\approx 0 \text{ for } z > z_c \ , \tag{39}$$

where $\alpha = \sqrt{Ri\frac{k^2+l^2}{k^2} - \frac{1}{4}}$. We take $\epsilon \mathbf{k} \mathbf{U}_0 > 0$ to impose an upward group velocity. In Eqs. (38)-(39) the GWs reflected or transmitted at $z_c$ have been neglected because $R_i \approx 6 \gg 0.25$ (Booker and Bretherton 1967). Note that Eq. (38) is an exact solution of Eq. (37) for the entire domain under $z_c$. Besides, the mean stress satisfies

$$\overline{\mathbf{u}'w'} \equiv \frac{1}{\pi L^2} \int_{-\infty}^{+\infty} \int_{-\infty}^{+\infty} \mathbf{u}'\, w'\, dx dy = \frac{4\pi^2}{\pi L^2} \int_{k=0}^{+\infty} \int_{l=-\infty}^{+\infty} (\hat{\mathbf{u}}\hat{w}^* + \hat{\mathbf{u}}^*\hat{w})\, dl\, dk \ . \tag{40}$$

We take the background wind of Eq. (3) for a cold front ($V_0 < 0, \Lambda > 0$), and use Eqs. (38)-(39) and the dispersion relationships for the GWs, which yields

$$\overline{\mathbf{u}'w'}(z) = \frac{8\pi^2}{\pi L^2} \int_{k=0}^{+\infty} \int_{l=-\frac{k\,U(z)}{V_0}}^{+\infty} -\frac{\mathbf{k}}{\|\mathbf{k}\|}(\mathbf{k}\mathbf{U}_0)\, N|\hat{h}'|^2 dl\, dk + \dots \ , \tag{41}$$

where the dots are for the $z$-independent part of the flux carried by the GWs that do not encounter critical levels. Then, the associated force is :

$$\overline{\mathcal{F}}(z) = -\frac{d}{dz}\overline{\mathbf{u}'\,w'} = \frac{8\pi^2}{\pi L^2}\, N\Lambda \cdot \int_0^{+\infty} k^2 \left|\hat{h}'(k, l = -k\frac{U(z)}{V_0})\right|^2 dk \cdot \frac{\Lambda z}{\|\mathbf{U}(z)\|}\left(\mathbf{e}_x - \frac{U(z)}{V_0}\mathbf{e}_y\right) \tag{42}$$

This last formula is valid for any kind of front of the form of Eq. (3), cold or warm. For the idealized orography profile of Eq. (1), $h' = \mathcal{H}(\mathbf{x})\cos(\mathbf{k}_w\mathbf{x})$, which leads to

$$\hat{h}' = \frac{H_0 L^2}{4\pi}\left(e^{-(\mathbf{k}-\mathbf{k}_w)^2\frac{L^2}{2}} + e^{-(\mathbf{k}+\mathbf{k}_w)^2\frac{L^2}{2}}\right). \tag{43}$$

To simplify the analytical treatment under the assumption that the horizontal scales are clearly separable ($\|\mathbf{k}_w\|L \gg 1$), we neglect the second gaussian term of Eq. (43), because it is centered around $-\mathbf{k}_w$ and the integral in Eq. (42) is for $k > 0$. The steepest descent estimate of the integral of the remaining gaussian term in Eq. (42) yields the Eqs. (22)-(23) in Section 2.3. Note that if $k_w\, l_w < 0$ for the cold front case, coherently we obtain $\overline{\mathcal{F}} \approx \mathbf{0}$, because the waves which encounter a critical level have a very small amplitude in this case. On the opposite, in the warm front case, $\overline{\mathcal{F}} \approx \mathbf{0}$ if $k_w\, l_w > 0$.

# References

Aebischer, U. and C. Schär, 1998: Low-level potential vorticity and cyclogenesis to the lee of the alps. *J. Atmos. Sci.*, **55(2)**, 186–207.

Binder, P. and C. Schär, 1996: The mesoscale alpine program map: Design proposal. 77p, available from http://www.map.ethz.ch/proposal.html.

Boer, G. J., N. A. McFarlane, R. Laprise, J. D. Henderson, and J.-P. Blanchet, 1984: The canadian climate center spectral atmospheric general circulation model. *Atmos.-Ocean.*, **22**, 397–429.

Booker, J. R., and F. P. Bretherton, 1967: The critical layer for internal gravity waves in a shear flow. *J. Fluid Mech.*, **27(3)**, 513–539.

Bougeault, P., P. Binder, A. Buzzi, R. Dirks, R. Houze, J. Kuettner, R. B. Smith, R. Steinacker, and H. Volkert, 2001: The map special observing period. *Bull. Amer. Meteor. Soc.*, **82**, 433–462.

Bretherton, F. P., 1969: Momentum transport by gravity waves. *Quart. J. Royal Meteor. Soc.*, **95(404)**, 213–243.

Broad, A. S., 1999: Do orographic gravity waves break in flows with uniform wind direction turning with height ? *Quart. J. Royal Meteor. Soc.*, **125**, 1695–1714.

Bühler, O., and M. E. McIntyre, 2005: Wave capture and wave-vortex duality. *J. Fluid Mech.*, **534**, 67–95.

Davis, C. A., 1997 The modification of baroclinic waves by the rocky mountains. *J. Atmos. Sci.*, **54**, 848–868.

Eliassen, A. and E. Palm, 1961: On the transfer of energy in the stationnary mountain waves. *Geophys. Publ.*, **22(3)**, 1–23.

Fantini, M. and S. Davolio, May 2001: Instability of neutral eady waves and orography. *J. Atmos. Sci.*, **58**, 1146–1154.

Flamant, C., E. Richard, C. Schär, R. Rotunno, L. Nance, M. Sprenger, and R. Benoit, 2004: The wake south of the alps: Dynamics and structure of the lee-side flow and secondary potential vorticity banners. *Quart. J. Royal Meteor. Soc.*, **130**, 1275–1303.

Gregory, D., G. J. Shutts, and J. R. Mitchell, 1998: A new gravity-wave-drag scheme incorporating anisotropic orography and low-level wave-breaking: Impact upon the climate of the uk meteorological office unified model. *Quart. J. Royal Meteor. Soc.*, **124**, 463–493.

Gross, B. D., 1994: Frontal interaction with isolated orography. *J. Atmos. Sci.*, **51(11)**, 1480–1496.

Haynes, P. H. and M. E. McIntyre", 1987: On the evolution of vorticity and potential vorticity in the presence of diabatic heating and frictional or other forces. *J. Atmos. Sci.*, **44(5)**, 828–841.

Hoinka, K. P., E. Richard, G. Poberaj, R. Busen, J.-L. Caccia, A. Fix, and H. Mannstein, 2003: Analysis of a potential-vorticity streamer crossing the alps during map iop 15 on 6 november 1999. *Quart. J. Royal Meteor. Soc.*, **129**, 609–632.

Hoskins, B. J., 1975: The geostrophic momentum approximation and the semi-geostrophic equations. *J. Atmos. Sci.*, **32(2)**, 233–242.

Hoskins, B. J. and M. E. McIntyre and A. W. Robertson, 1985: On the use and significance of isentropic potential vorticity maps. *Quart. J. Royal Meteor. Soc.*, **111**, 877–946.

Jiang, Q. and J. D. Doyle, 2004: Gravity wave breaking over the central alps: role of complex terrain. *J. Atmos. Sci.*, **61**, 2249–2266.

Liniger, M. A. and H. C. Davies, 2003: Substructure of a map streamer. *Quart. J. Royal Meteor. Soc.*, **129**, 633–651.

Lott, F. and M. J. Miller, 1997: A new subrig-scale orographic parametrization: Its formulation and testing. *Quart. J. Royal Meteor. Soc.*, **123**, 101–127.

Lott, F., 1999: Alleviation of stationary biases in a gcm through a mountain drag parametrization scheme and a simple representation of mountain lift forces. *Mon. Wea. Rev.*, **127**, 788–801.

Lott, F., 2003 Large scale flow response to short gravity waves breaking in a rotating shear flow. *J. Atmos. Sci.*, **60**, 1691–1704.

McFarlane, N. A., 1987: The effect of orographically excited gravity wave drag on the general circulation of the lower stratosphere and troposphere. *J. Atmos. Sci.*, **44**, 1775–1800.

Messinger, M. and R. Pierrehumbert, 1986: Alpine lee cyclogenesis: numerical simulation and theory. *Scientific Results of the Alpine Experiment*, VolI, GARP Publications Series **27**, 141–165.

Miller, M. J., T. N. Palmer, and R. Swinbank, 1989: Parametrization and influence of subgridscale orography in general circulation and numerical weather prediction models. *Meteorology and Atmos. Physics*, **40**, 84–109.

Palmer, T.N., G. J. Shutts, and R. Swinbank, 1986: Alleviation of a systematic westerly bias in general circulation and numerical weather prediction models through an orographic gravity wave drag parametrization. *Quart. J. Royal Meteor. Soc.*, **112**, 1001–1039.

Phillips, D. S., 1984: Analytical surface pressure and drag for linear hydrostatic flow over three-dimensional elliptical mountains. *J. Atmos. Sci.*, **41**, 1073–1084.

Pierrehumbert, R. T., 1985: A theoretical model of orographically modified cyclogenesis. *J. Atmos. Sci.*, **42(12)**, 1244–1258.

Plougonven, R. and D. J., Muraki and C. Snyder, 2005: A baroclinic instability that couples balanced motions and gravity waves. *J. Atmos. Sci.*, **62**, 1545–1559.

Scavuzzo, C. M., M. A. Lamfri, H. Teitelbaum, and F. Lott, 1998: A study of the low frequency inertio-gravity waves observed during PYREX. *J. of Geophysical Research*, **103(D2)**, 1747–1758.

Schär., C., 1990: Quasi-geostrophic lee cyclogenesis. *J. Atmos. Sci.*, **47(24)**, 3044–3066.

Schär, C. and D. R. Durran, 1997: Vortex formation and vortex shedding in continuously stratified flows past isolated topography. *J. Atmos. Sci.*, **54(4)**, 533–554.

Schär, C., M. Sprenger, D. Lüthi, Q. Jiang, R. B. Smith, and R. Benoit, 2003: Structure and dynamics of an alpine potential-vorticity banner. *Quart. J. Royal Meteor. Soc.*, **129**, 825–855.

Scinocca, J. F., and N. A. McFarlane, 2000: The parametrization of drag induced by stratitified flow over anisotropic orography. *Quart. J. Royal Meteor. Soc.*, **126(568)**, 2353–2393.

Shutts, G. J., 1995: Gravity-wave drag parametrization over complex terrain: the effect of critical-level absorption in directional wind-shear. *Quart. J. Royal Meteor. Soc.*, **121**, 1005–1021.

Shutts, G. J., and A. Gadian 1998: Numerical simulations of orographic gravity waves in flows which back with height. *Quart. J. Royal Meteor. Soc.*, **125**, 2743–2765.

Shutts, G. J., 2003: Inertia-gravity wave and neutral eady wave trains forced by directionnally sheared flow over isolated hills. *J. Atmos. Sci.*, **60(4)**, 593–606.

Smith, R. B., 1979 Some aspects of the quasi-geostrophic flow over mountains. *J. Atmos. Sci.*, **36**, 2385–2393.

Smith, R. B., 1984: A theory of lee cyclogenesis. *J. Atmos. Sci.*, **41(7)**, 1159–1168.

Smith, R. B., 1986: Further development of a theory of lee cyclogenesis. *J. Atmos. Sci.*, **43(15)**, 1582–1602.

Speranza, A., A. Buzzi, A. Trevisan, and P. Malguzzi, 1985: A theory of deep cyclogenesis in the lee of the alps. part i: Modifications of baroclinic instability by localized topography. *J. Atmos. Sci.*, **42**, 1521–1535.

Vadas, S. L., D. C. Fritts, and M. J. Alexander, 2003: Mechanism for the generation of secondary waves in wave breaking regions. *J. Atmos. Sci.*, **60**, 194–214.

Webster, S., A. R. Brown, D. R. Cameron, and C. P. Jones, 2003: Improvements to the representation of orography in the met office unified model. *Quart. J. Royal Meteor. Soc.*, **129**, 1989–2010.
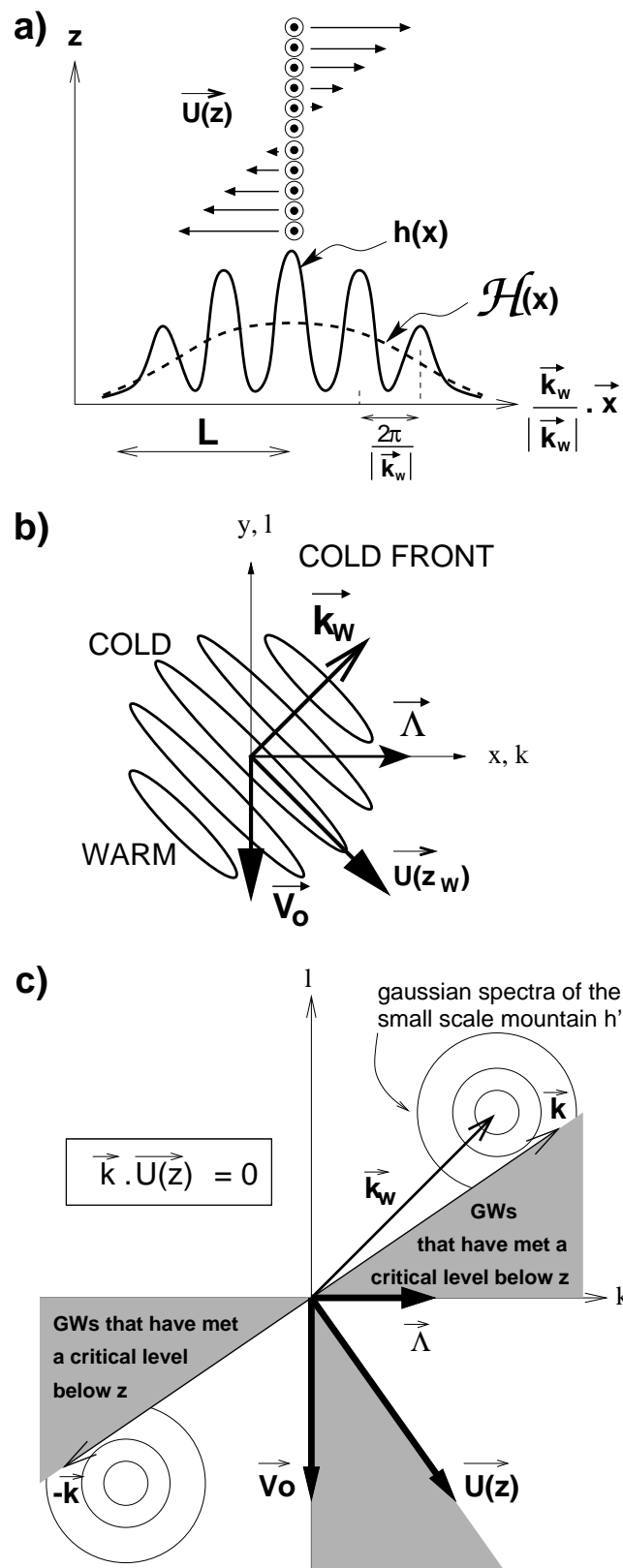
Figure 1: Schematic representation of the idealized mountain range and of the background flow used to derive the model equations in the cold front case: a) vertical section with horizontal axis along $\mathbf{k}_w$, b) view from top, c) spectrum of the small-scale orography $h' = \mathcal{H}(\mathbf{x}) \cos(\mathbf{k}_w \mathbf{x})$.
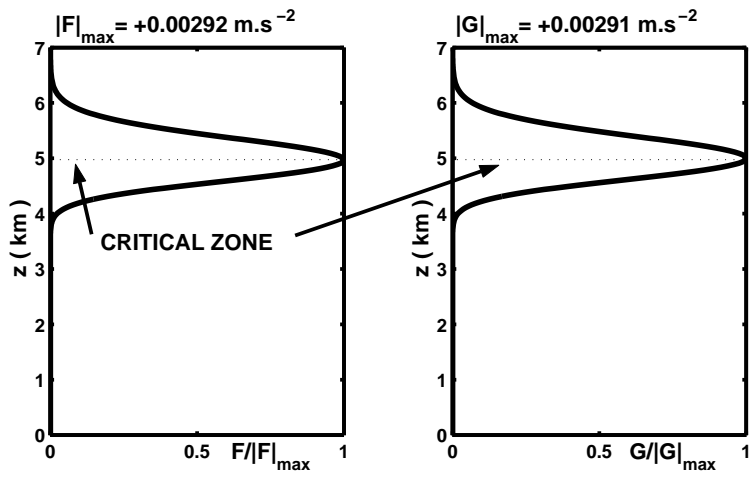
Figure 2: Vertical profile of the force $\overline{\mathcal{F}}(z)$ in the idealized cold front case in section 3 : $\theta_r = 300$ K, , $f = 10^{-4}$ s$^{-1}$, $N = 10^{-2}$ s$^{-1}$, $\Lambda = 4.10^{-3}$ s$^{-1}$, $U_0 = 0$ ms$^{-1}$, $V_0 = -20$ ms$^{-1}$, $H_0 = 800$ m, $L = 200$ km, $|\mathbf{k}_W| = \frac{2\pi}{70000}$ m$^{-1}$ and $k_w = l_w$.
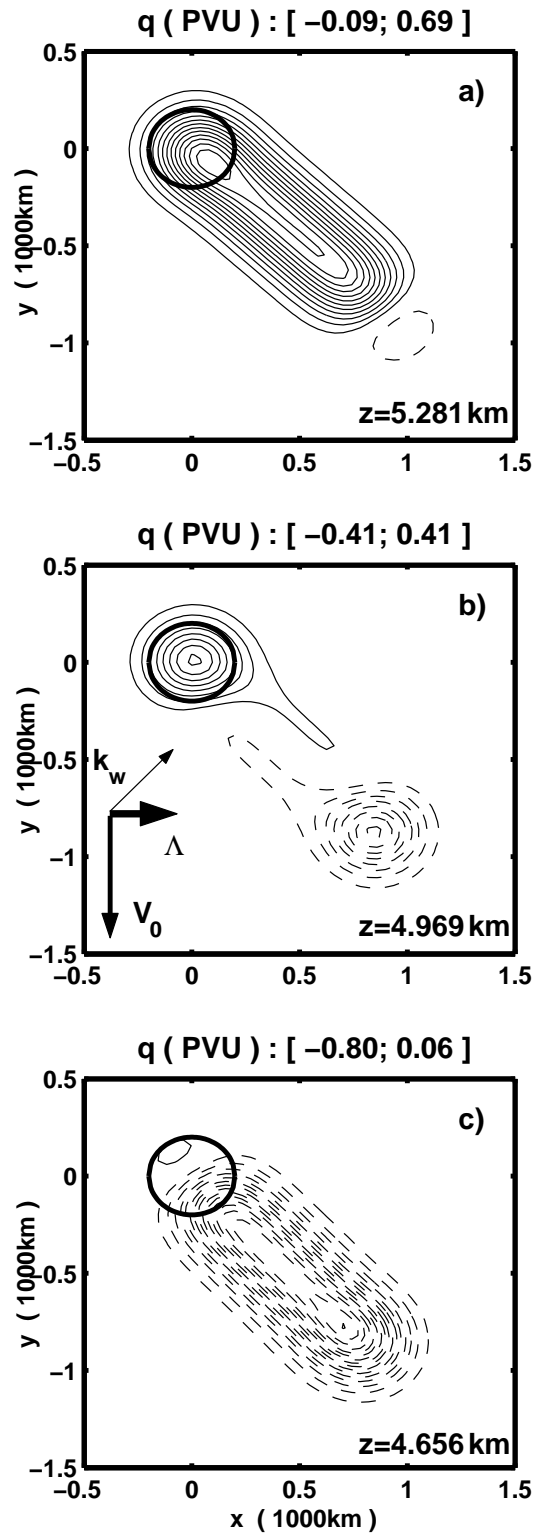
Figure 3: Horizontal sections of the PV anomaly in the critical zone, at t=12hrs, and for different heights: a) $z =5.281$km, b) $z =4.969$km, c) $z =4.656$km. Same parameters as in Fig. 2. CI=0.05 PVU, where 1 PVU=$1.0 * 10^{-6}\,\mathrm{K\,kg^{-1}\,m^2\,s^{-1}}$. Negative values dashed. The minimum and maximum values of $q$ are indicated above each panel. The location and half-height width of the mountain range is indicated by the circle.
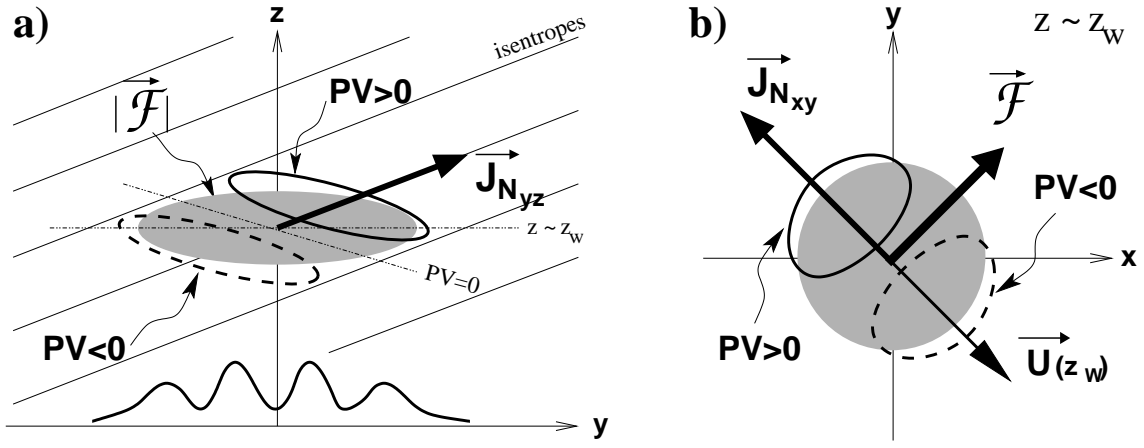
Figure 4: Schematic representation of the non advective PV flux $\mathbf{J}_N$ and of its effects on the PV. The PV lobes are schematized by the thick solid and dashed closed lines. The grey area represents the critical zone, that is the zone where the GWs' force $\mathcal{F}$ is substantial. a) Vertical section at $x = 0$: the tilted isentropes are also schematized by thin solid lines; b) Horizontal section at $z = z_w$.
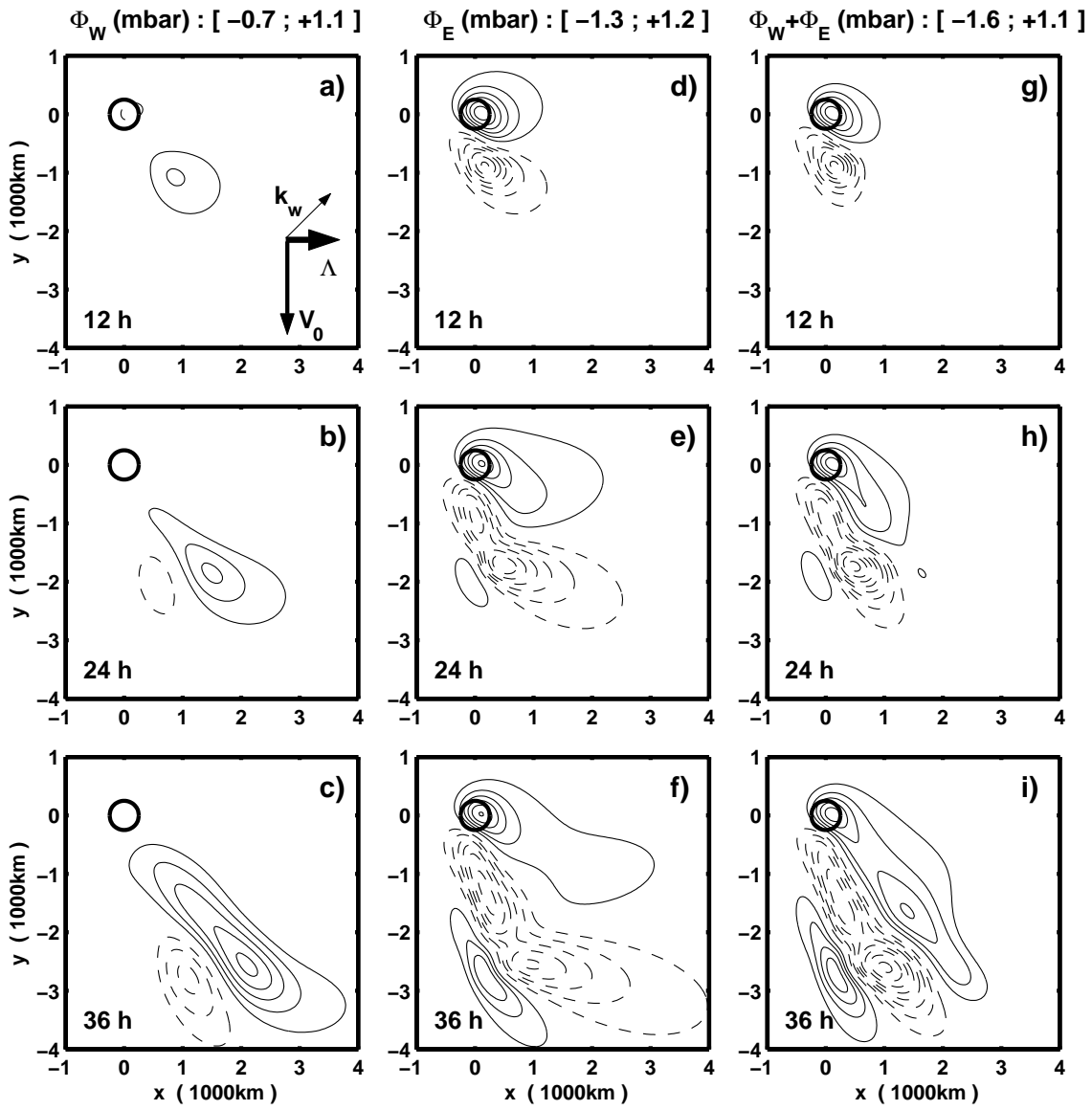
Figure 5: Evolution of the surface geopotentials at t=12hrs, 24hrs and 36hrs. Same parameters as in Fig. 2. a), b) and c) : geopotential due to the GWs ($\phi_W$); d), e) and f) : geopotential due to the large-scale orography profile $\mathcal{H}(\mathbf{x})$ ($\phi_E$); g), h) and i) : total perturbation ($\phi_W + \phi_E$). The magnitude is indicated in mb, as a pressure because $\rho_r = 1\,\mathrm{kg\,m^{-3}}$. CI=0.2mb, and negative values are dashed. The minimum and maximum values reached at t=36hrs are indicated at the top of each column. The configuration of the background front as regards to the orientation of the ridges is schematized in a).
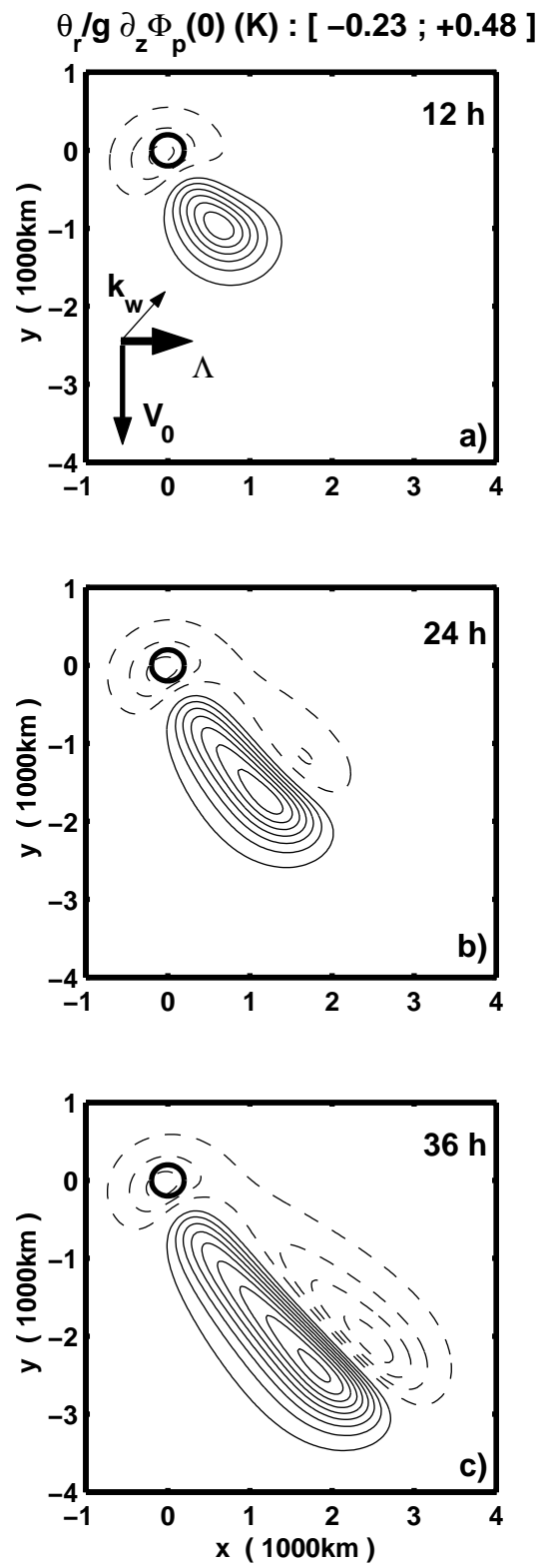
Figure 6: Evolution of the potential temperature anomaly at the surface $\frac{\theta_r}{g}\partial_z\phi_p(0)$. Same parameters as in Fig. 2. a) t=12hrs, b) t=24hrs, c) t=36hrs. CI=0.5K, negative values are dashed.
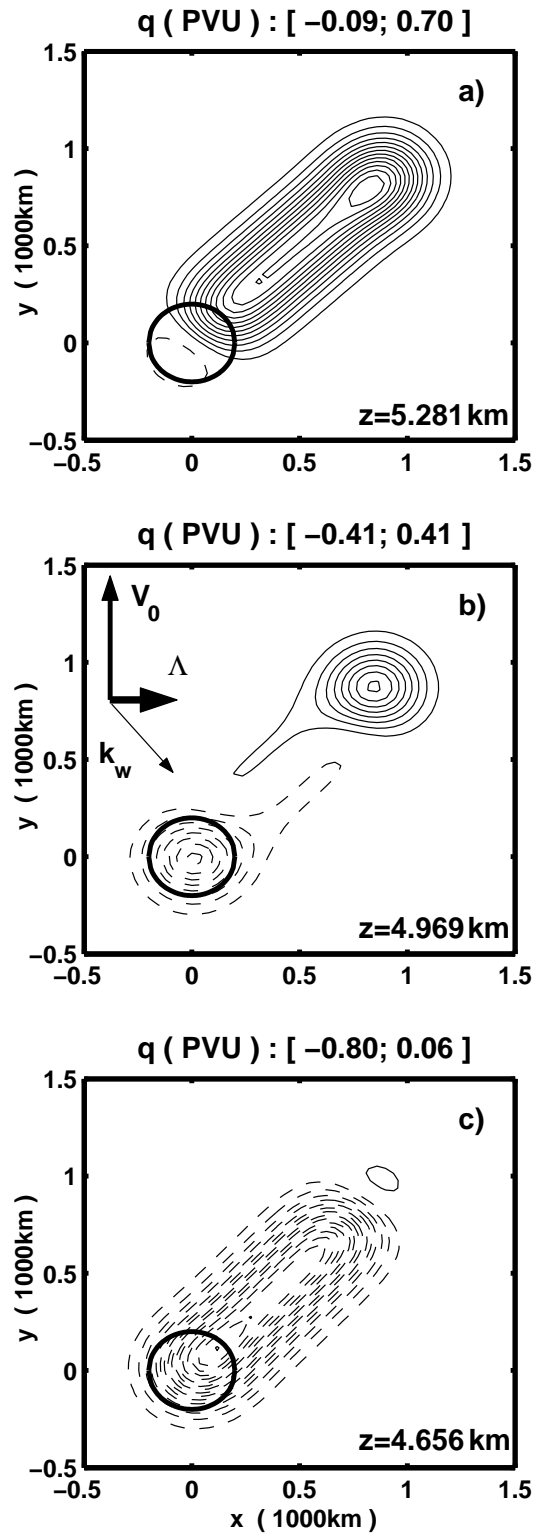
Figure 7: Horizontal sections of the PV anomaly in the critical zone at $t = 12hrs$ and for different heights, for the warm front case in section 4 : a) $z =$5.281km, b) $z =$4.969km, c) $z =$4.656km. Same parameters as in Fig. 2 except $V_0 = 20\,\mathrm{ms^{-1}}$ and $k_w = -l_w$. CI=0.05 PVU, negative values are dashed.
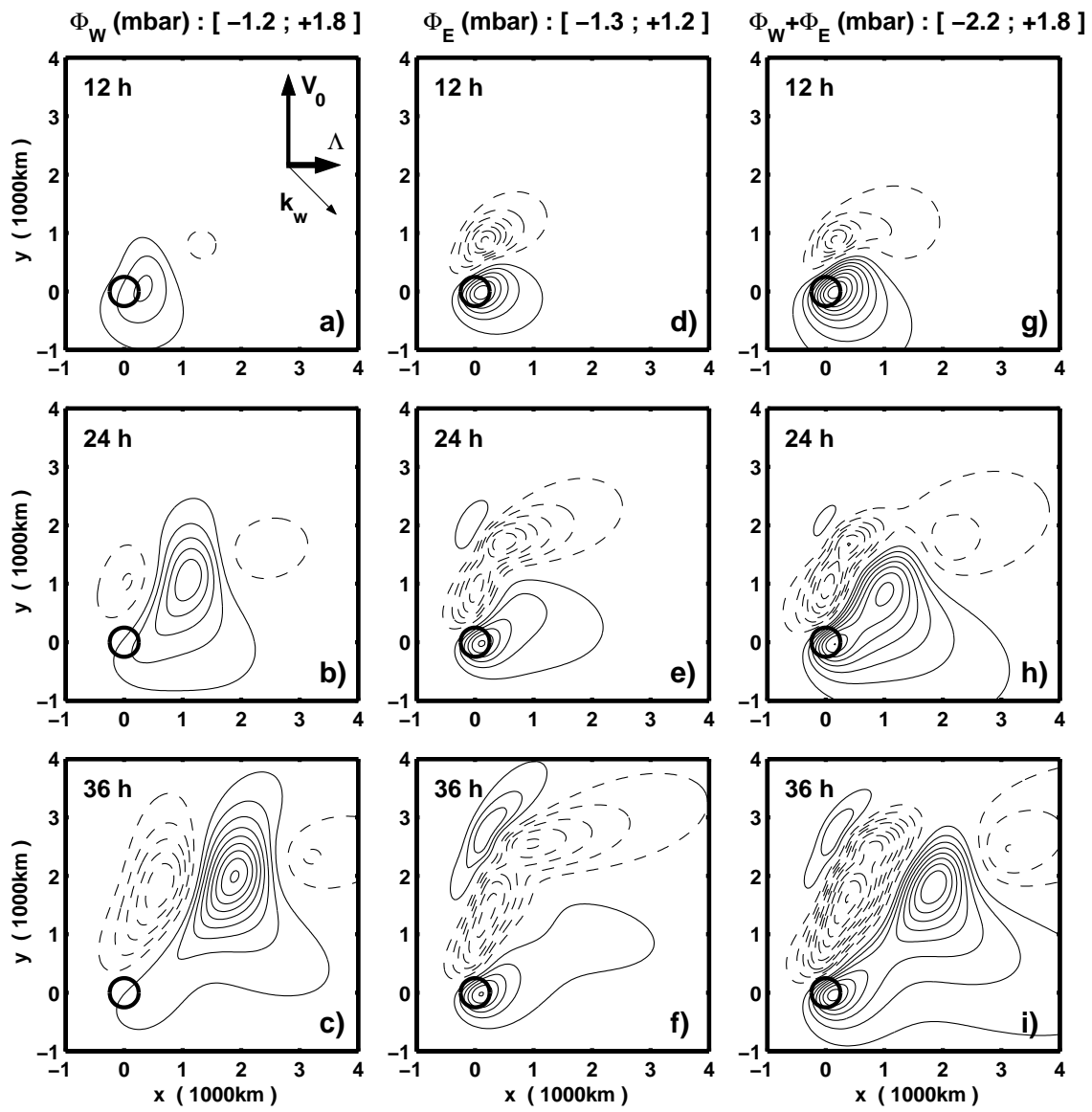
Figure 8: Same as in Fig.5 but in the warm front case (same parameters as in Fig. 7).
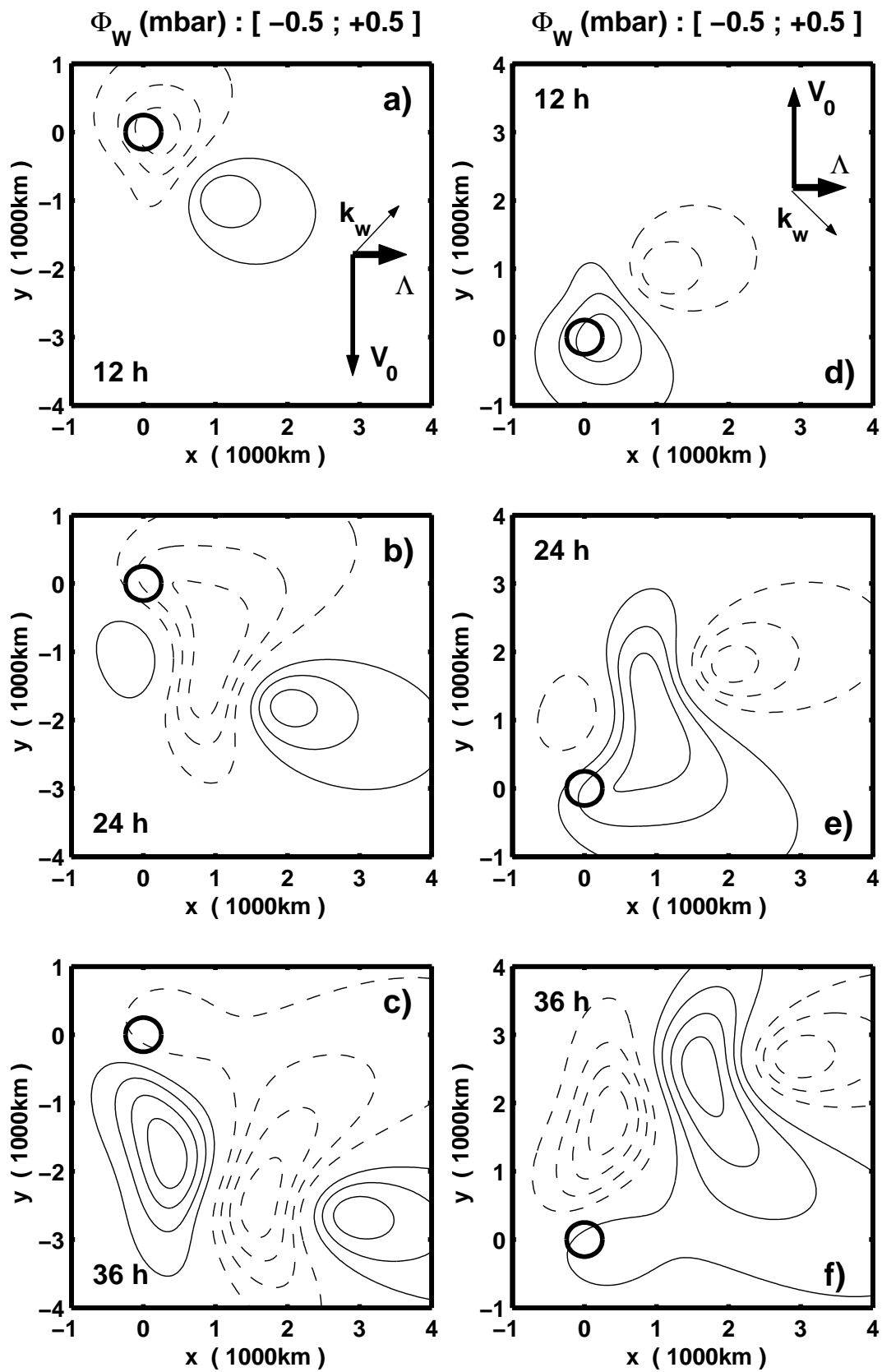
Figure 9: Quasi-geostrophic response to the GWs force: a), b) and c) Cold front, same parameters as in Fig.5; d), e) and f) Warm front, same parameters as in Fig.8. CI=0.1mb, negative values are dashed.
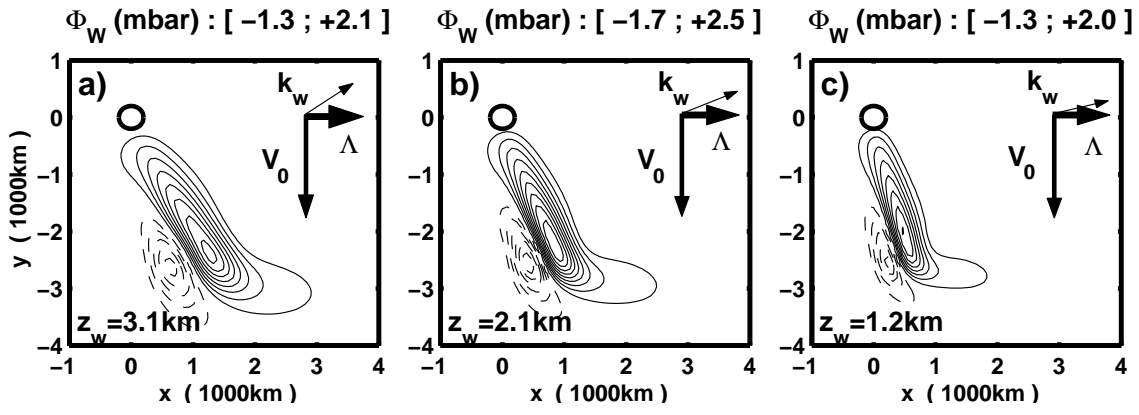
Figure 10: Surface geopotential $\phi_W$ induced by the GWs at t=36hrs for three different orientations $(\widehat{\mathbf{e}_x; \mathbf{k}_w})$, and for the cold front in section 3. Same background flow and orography parameters as in Fig. 2 except: a) $(\widehat{\mathbf{e}_x; \mathbf{k}_w}) = 0.7\frac{\pi}{4}$, b) $(\widehat{\mathbf{e}_x; \mathbf{k}_w}) = 0.5\frac{\pi}{4}$, and c) $(\widehat{\mathbf{e}_x; \mathbf{k}_w}) = 0.3\frac{\pi}{4}$. The corresponding altitude of the critical zone is also indicated. CI=0.25 mb.
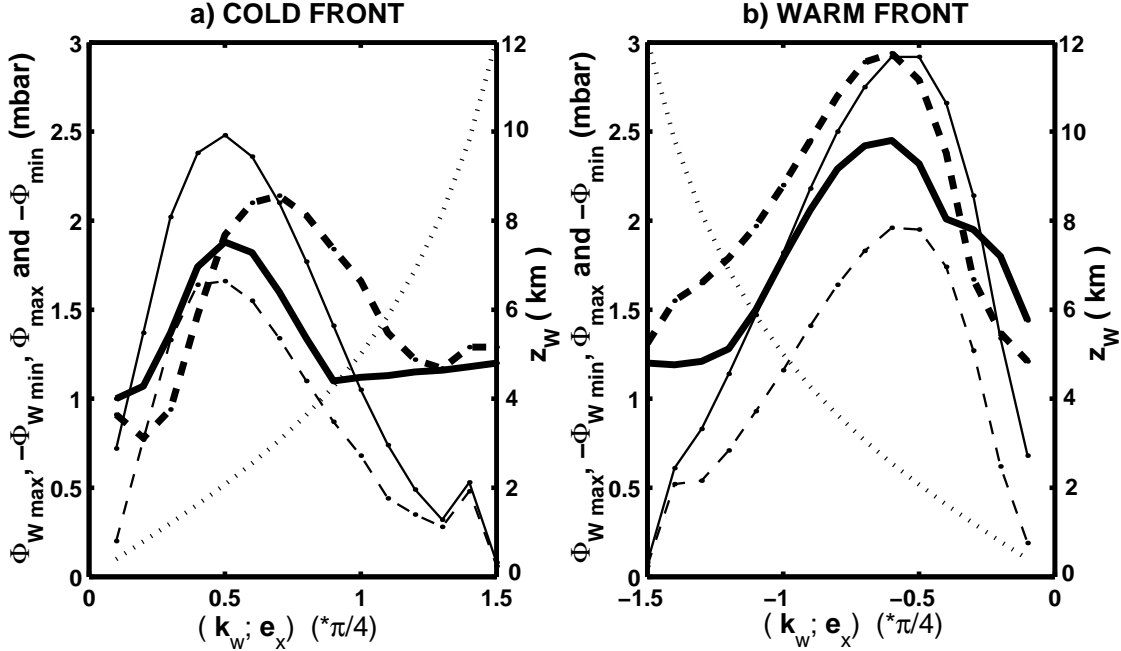


Figure 11: Extrema in the surface geopotential due to the GWs at t=36hrs and for various angles $(\widehat{\mathbf{e}_x; \mathbf{k}_w})$: a) Cold front, b) warm front. In both a) and b): Max($\phi_W$) (thin solid), $-$Min($\phi_W$) (thin dashed), Max($\phi_W + \phi_E$) (thick solid), $-$Min($\phi_W + \phi_E$) (thick dashed), and $z_w$ (dotted line).
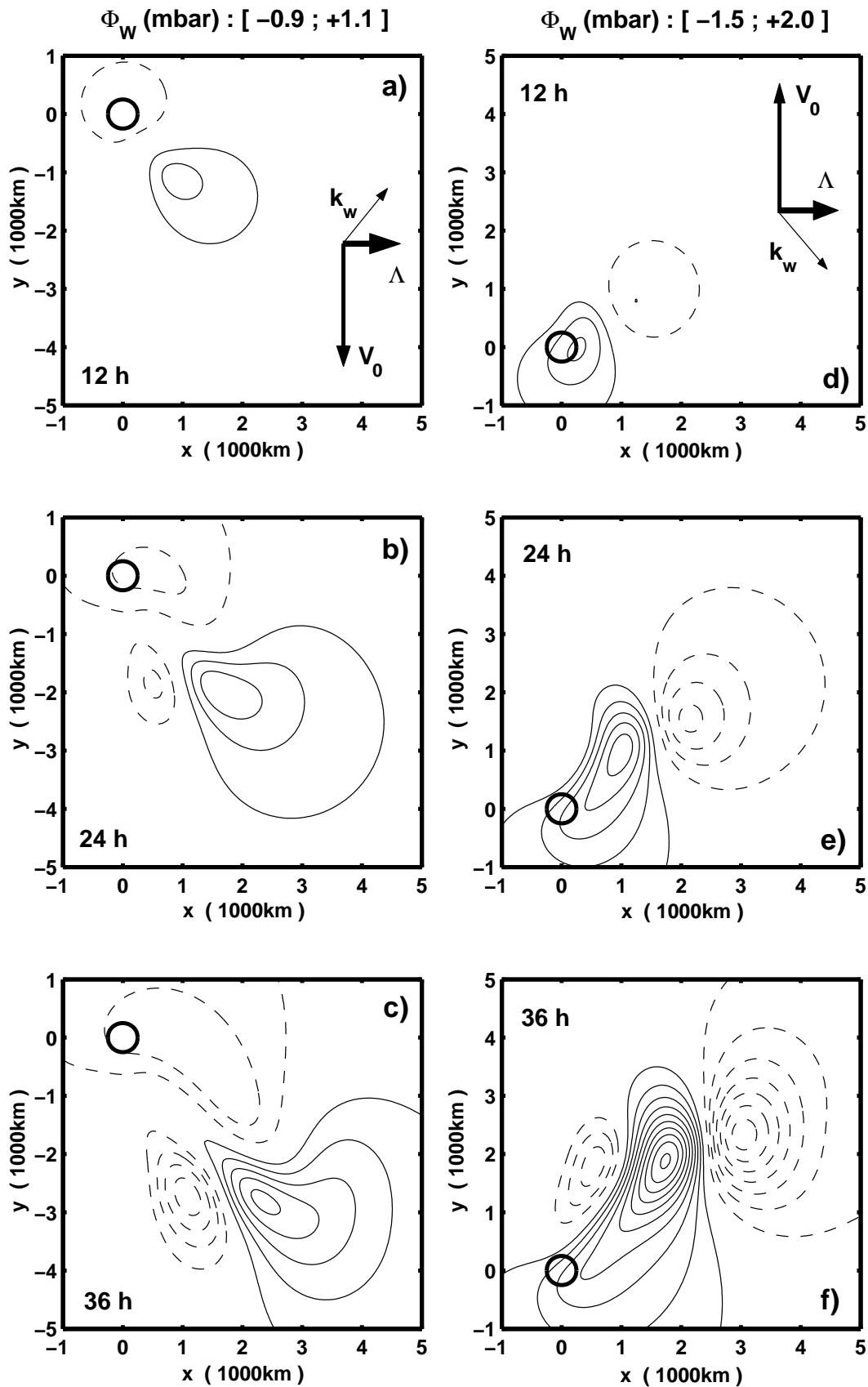
Figure 12: Simulations with a tropopause at D=10km. Cold front with the same parameters as in Fig. 5: a) t=12hrs, b) t=24hrs and c) t=36hrs; Warm front with the same parameters as in Fig. 8: d) t=12hrs, e) t=24hrs and f) t=36hrs. CI=0.2mb, negative values are dashed.
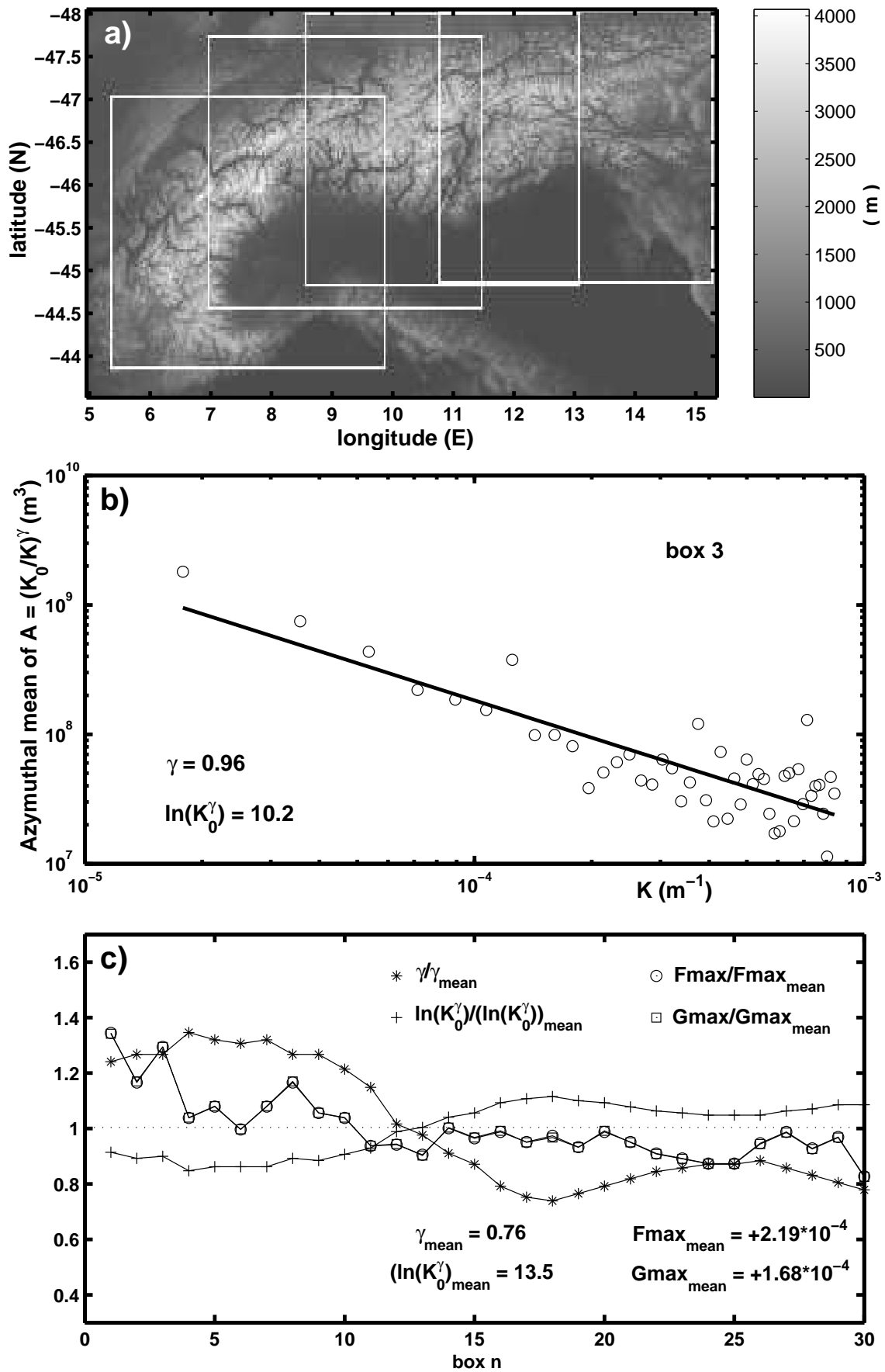
Figure 13: Spectral analysis of the Alps. a) Elevation from ETOPO2. Five among the thirty boxes used to evaluate the mean spectrum are indicated for illustration. b) Azimuthal mean of the periodigram (circles) and best square linear fit (thick solid) for the box 3 shown in the lower left of a). c) Best fit values for the 30 boxes: $\gamma$ (solid and star), $\ln(K_0^{\gamma})$ (solid and plus), $\mathcal{F}_{max}$ (solid and circles), and $\mathcal{G}_{max}$ (solid and square). All values in c) are divided by their mean value over the 30 boxes.
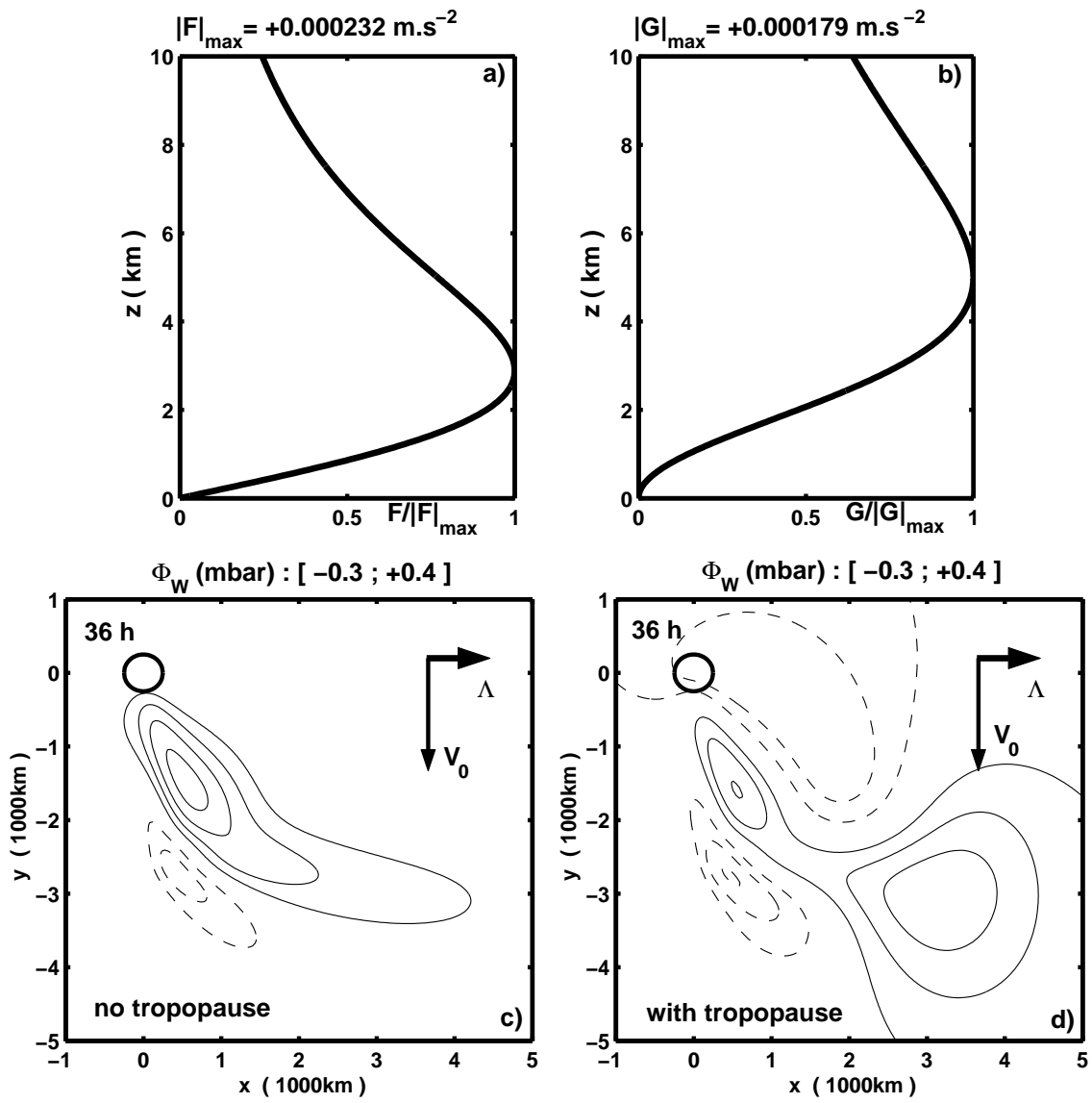
Figure 14: Cold front simulations with an orographic spectrum representative of the Alps. a) Vertical profile of $\overline{\mathcal{F}}(z)$, b) Vertical profile of $\overline{\mathcal{G}}(z)$, c) $\phi_W$ at t=36hrs: no tropopause, and $\phi_W$ at t=36hrs: tropopause in $D$ =10km. CI=0.1mb, negative values are dashed.